

# Passive Microwave Remote Sensing of the Earth from Space—A Review

ENI G. NJOKU, MEMBER, IEEE

**Abstract**—During the past decade, microwave radiometry from space has developed into a powerful technique for remote sensing of the earth's atmosphere and surface. Passive microwave sensors on earth-orbiting satellites are beginning to make significant contributions to the fields of operational meteorology and oceanography. This paper reviews the development of microwave radiometry from space as a tool for several atmospheric and surface remote-sensing applications. The basic spacecraft radiometer system concepts are discussed and a description of the key individual sensors launched prior to 1981 is provided along with their significant results. Recent studies on new instrument designs and potential applications are summarized, and indicate the unique possibilities for future implementation of passive microwave techniques.

## I. INTRODUCTION

IN RECENT YEARS there has been growing interest in the use of microwave and millimeter-wave radiometry for remote sensing of the earth from space. Some applications have become well established, such as temperature sounding for meteorological purposes and sea-ice mapping for navigation in polar regions. Other applications are still in the demonstration phase, such as measurements of surface temperature and wind speed over the oceans. The potential applications of radiometry from space have proliferated rapidly in the past decade, and include observations of surface features over ocean, land, and ice regions, and the monitoring of phenomena in the lower and upper regions of the atmosphere. To develop these applications for scientific, government, and commercial requirements a number of microwave radiometer systems have been designed over the past several years and successfully operated in space, and other more advanced systems are in the planning stages. Staelin [1], [2] and Tomiyasu [3] have reviewed the progress in development of techniques for passive microwave earth observations. The present paper reviews the progress to date in implementation of these techniques using satellite sensors. A brief discussion of the historical development of microwave radiometry from space is provided followed by a review of radiometer system concepts as applied to spacecraft platforms. The microwave radiometric sensors launched on the Nimbus satellites, Skylab, and Seasat are discussed with a summary of the important results from each sensor. Finally, future development concepts are discussed with reference to new applications and operational demonstrations.

## II. BACKGROUND

### A. Historical Development

Subsequent to the early ground-based passive microwave observations of the atmosphere by Dicke *et al.* [4] it was realized that the use of radiometers in space for microwave observations

Manuscript received September 4, 1981; revised March 19, 1982. This research was carried out by the Jet Propulsion Laboratory, California Institute of Technology, under Contract with the National Aeronautics and Space Administration.

The author is with the Jet Propulsion Laboratory, California Institute of Technology, Pasadena, CA 91103.

of the earth's emitted radiation was a valuable means for studying global properties of the earth's atmosphere and surface. The first test however of a spacecraft microwave radiometer was on the Mariner 2 Venus flyby mission of December 1962. The microwave radiometer aboard the spacecraft successfully measured emission from the planet at frequencies of 15.8 and 22.2 GHz on three scans of the planetary disk [5]. Results showed that the planetary emission was characterized by limb-darkening, and confirmed the high surface temperature of Venus.

The application of microwave radiometry from space to remote sensing of the earth began with observations from the Soviet satellite Cosmos 243 which was launched into an elliptical orbit around the earth on September 23, 1968. Measurements were made at frequencies of 3.5, 8.8, 22.2, and 37.5 GHz in a nonscanning, nadir-viewing mode, from which estimates of atmospheric water vapor, liquid water, sea temperature, and ice cover were made [6]. This was followed by a series of earth-viewing radiometers on both U.S. and Soviet satellites. The most extensive observations to date have been made by radiometers on the Nimbus series of satellites. Microwave radiometers launched prior to 1981 are listed in Table I with brief descriptions of their characteristics. These radiometers, and a well-established program of supporting research and aircraft radiometer flights, have helped to demonstrate the growing potential of microwave radiometry for operational remote sensing from space.

In progressing toward the development of operational spaceborne remote sensors, two kinds of system have evolved. Atmospheric sounders provide information about vertical profiles of temperature and molecular constituents in the atmosphere by making measurements near the molecular resonance frequencies. Surface sensors, on the other hand, operate primarily at window frequencies, where atmospheric absorption is low and surface features can be imaged or measured quantitatively. For most of these surface features high spatial resolution is desirable. For both sounders and surface sensors the microwave instruments have a distinct advantage over their counterparts at infrared or visible wavelengths in that the presence of most cloud cover does not significantly degrade the measurement accuracy. Thus microwave measurements from orbit provide a global, day or night, nearly all-weather remote-sensing capability. These advantages, together with the unique signatures of some surface and atmospheric features at microwave wavelengths, have encouraged the development of spacecraft passive microwave sensors in recent years.

Fig. 1 shows the microwave absorption spectrum of the earth's atmosphere [7]. The two curves give the zenith opacity, calculated using the 1962 U.S. Standard Atmosphere, for the primary absorbing constituents: water vapor, oxygen, and ozone. The lower curve is for no water vapor, while the upper curve is for  $2\text{-g}/\text{cm}^2$  total water vapor (assuming a water vapor density of  $10\text{ g}/\text{m}^3$  at the surface, decreasing exponentially with

TABLE I  
History of Microwave Radiometry on Spacecraft  
(Adapted from Staelin [2].)

Year of Launch	Spacecraft	Instrument Acronym	Frequencies (GHz)	Antenna Type	Swath Width of Scan (km)	Smallest Resolution Element (km)	Principal Parameters Measured or Inferred
1962	Mariner 2 (Venus flyby)	—	15.8, 22.2	Mechanically scanned parabola	Planetary	1300	Limb darkening of planetary emission, temperature
1968	Cosmos 243	—	3.5, 8.8	Nadir-viewing parabola	—	13	Atmosphere: Water vapor content, liquid water content Surface: Sea temperature, sea ice concentration
1970	Cosmos 384	—	22.2, 37	—	—	—	Surface: Sea temperature, sea ice concentration
1972	Nimbus-5	ESMR	19.3	Electrically scanned array	3000	25	Atmosphere: Rain rate Surface: Sea ice concentration, ice classification
		NEMS	22.2, 31.4, 53.6, 54.9, 58.8	Five lens-loaded horns, nadir-viewing	—	200	Atmosphere: Temperature profile, water vapor content, liquid vapor content Surface: Ice classification, snow cover
1973	Skylab	S-193	13.9	Mechanically scanned parabola	180	16	Surface: winds, precipitation
		S-194	1.4	Nadir-viewing array	—	115	Surface: soil moisture
1974†	Meteor	—	37	Dual polarization 35° from nadir	—	—	Atmosphere: liquid water content
1975	Nimbus-6	ESMR	37	Electrically scanned array, dual-polarization	1300	20 x 43	Same as Nimbus-5 ESMR
		SCAMS	22.2, 31.6, 52.8, 53.8, 55.4	Three rotating hyperbolic mirrors	2700	150	Same as Nimbus-5 NEMS
1978†	Block 5D	SSM/T	50.5, 53.2, 54.3, 54.9, 58.4, 58.8, 59.4	Single rotating mirror	1600	175	Atmosphere: Temperature profile
1978†	Tiros-N (2 satellites)	MSU	50.3, 53.7, 55.0, 57.9	Dual rotating mirrors	2300	110	Atmosphere: Temperature profile
1978	Seasat	SMMR	6.6, 10.7, 18, 21, 37	Offset-fed oscillating parabola, dual-polarization	600	18 x 28	Atmosphere: Water vapor content, liquid water content, rain rate Surface: Sea temperature, wind speed, sea ice concentration, ice classification, snow cover, soil moisture
1978	Nimbus-7	—	—	—	800	22 x 35	—

† Additional launches in subsequent years.

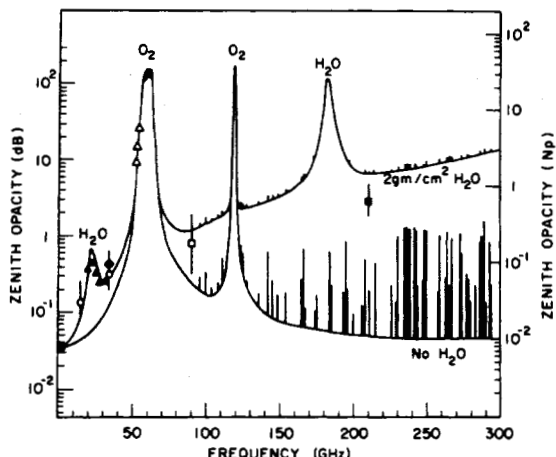


Fig. 1. Microwave absorption spectrum of the earth's atmosphere for constituents water vapor, oxygen, and ozone (after Waters [7]).

a scale height of 2 km). Also shown are some measured values as discussed in [7].

### B. Atmospheric Sounding

One of the earliest meteorological applications of spaceborne radiometry was in global atmospheric temperature sounding. The mixing ratio of oxygen in the atmosphere is quite uniform and time-invariant, thus measurements of atmospheric emission at frequencies around the oxygen resonance complex (centered near 60 GHz) are proportional to atmospheric temperature at altitude levels defined by temperature weighting functions [8], [9]. By choosing frequencies whose weighting functions peak at different altitudes, retrieval techniques can be used to estimate vertical temperature profiles by inversion of the microwave data [10], [11].

The Nimbus-5 Microwave Spectrometer (NEMS) was the first instrument of this type, with three oxygen channels for temperature sounding. Since the weighting functions are weakly dependent on atmospheric water content and surface reflectivity, two additional channels were added, one on the water vapor absorption line (22.2 GHz) and one at a window frequency (31.4 GHz). Results from NEMS have been reported by Waters *et al.* [11], and Staelin *et al.* [12], [13]. A second instrument of this type, the Scanning Microwave Spectrometer (SCAMS), was flown on Nimbus-6. SCAMS provided global maps of atmospheric temperature structure and further demonstrated the feasibility of the technique for studying meteorological phenomena [14], [15]. The success of these two experimental sensors led to the development of microwave temperature sounders for operational use in synoptic meteorology. One of these is the four-channel Microwave Sounding Unit (MSU) launched on the TIROS-N satellite series. Another is a seven-channel microwave temperature sounder (SSM/T) operated on the Defense Meteorological Satellite Program (DMSP) Block 5D satellite.

Techniques are presently being studied to use resonances other than the oxygen 60-GHz complex for atmospheric temperature and composition sounding. The oxygen line at 118 GHz shows promise for temperature sounding from geosynchronous orbit, since the higher frequency reduces the antenna size required to achieve satisfactory spatial resolution from that altitude. The 183-GHz water vapor line is sensitive to changes in atmospheric water vapor gradients above about 2 km. Thus measurements around this frequency may be used to study the

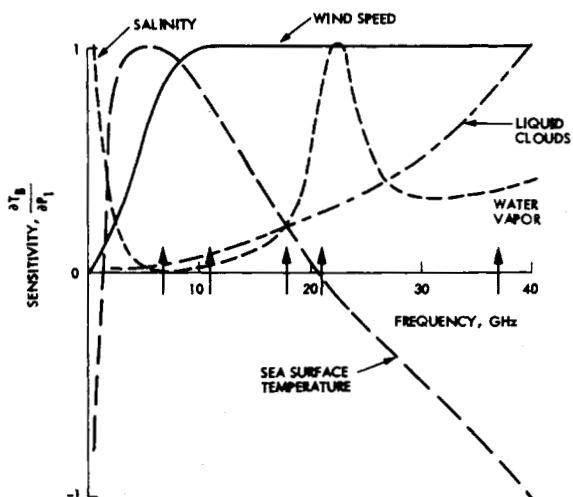


Fig. 2. Normalized sensitivity of brightness temperature ( $T_B$ ) to various geophysical parameters ( $P_i$ ) as a function of frequency (schematic). Arrows indicate SMMR frequencies (after Wilheit *et al.* [19]).

vertical distribution of water vapor. Measurements of temperature and water vapor profiles from geosynchronous orbit are necessary for future operational severe-storm monitoring from space [16].

Another approach to monitoring atmospheric constituents, particularly in the upper atmosphere, is the limb-sounding technique. This technique can provide substantially improved sensitivities and vertical resolution over downward-looking systems. Ozone in particular, among other molecular species, is known to have a marked effect on the earth's environment, and there is considerable incentive for measuring its spatial and temporal distribution. Limb-sounding radiometers operating at microwave and millimeter wavelengths are currently under development, and will enable global measurements of these species to be made [17].

### C. Surface Sensing

Surface-sensing applications can be divided into three main categories: Ocean, Ice, and Land. In general, atmospheric window frequencies are used to study the surface phenomena. However, measurements at these frequencies are affected to some extent by tropospheric water vapor, clouds, and rainfall. Hence most surface-sensing radiometer systems include frequency channels sensitive to atmospheric water vapor and liquid water, to measure global distributions of these parameters and to correct for their effects on the measurement of surface parameters. Microwave radiation from atmospheric liquid water and the earth's surface is by the mechanism of nonresonant thermal emission, thus the precise frequencies chosen to observe these parameters are usually noncritical. Frequencies are generally chosen to maximize sensitivity to particular parameters under different environmental conditions and to operate in regions of the spectrum free of interference from ground-based or earth-to-space radars and communication links.

For example, the SMRR (discussed in Section IV-G) is a five-frequency radiometer system designed primarily to measure sea-surface temperature, wind speed, and atmospheric water vapor and liquid water. Fig. 2 shows the sensitivities of the radiometer measurements (brightness temperatures,  $T_B$ ) to these four parameters and salinity, as functions of frequency. These curves are based on physical models of ocean and atmosphere microwave emission, as reviewed by Wilheit [18], [19],

and have been normalized for representation on the same scale. The SMMR frequencies are indicated on the frequency axis, and provide good sensitivity to and discrimination of the four required parameters while not being affected by variations in salinity. (Further discrimination is obtained by utilizing the polarization properties of the received radiation.) Physical models of microwave emission from ocean, ice, and land surfaces have been reviewed elsewhere in the literature [18]–[23] and will not be discussed at length here.

Radiometers on the Cosmos satellites, and the two low-frequency channels on NEMS and SCAMS, made the first measurements of atmospheric water vapor and cloud liquid water over the oceans [6], [13]. These measurements were possible due to the contrast between the warm radiative temperature of atmospheric water against the cold radiative background of the ocean. Against the warm background radiation over land, these measurements cannot be accurately made. The radiometers also measured sea-ice concentration, ice type, and snow cover [23]. The sea-ice measurements were substantially improved by measurements from the 19.35-GHz Electrically Scanning Microwave Radiometer (ESMR) on Nimbus-5 and the 37-GHz ESMR on Nimbus-6. The ESMR's provided medium resolution ( $\sim 35$  km) images of the polar ice, containing information on the variations of the ice packs on time scales ranging from several days to seasons [24]. The technique uses the large differences in emissivity and polarization properties of the various ice types, and of the neighboring sea water. Applications of such data for ship navigation and offshore engineering in polar regions and for climatological studies appear promising.

The ESMR instruments have also been used for global measurement of rainfall over the oceans. Rain has an enhanced effect on brightness temperature, over nonprecipitating liquid water, due to the larger droplet sizes than found in nonraining clouds, and due to the greater total water content in rain clouds. While quantitative measurements are difficult at present due to the complicated modeling problems involved, precipitation areas in the vicinity of storm systems have been identified, and relative global distributions of precipitation have been obtained [25], [26].

During 1973 and 1974 two microwave radiometers at 13.9 and 1.4 GHz were operated aboard the orbiting Skylab space station. Three short-duration missions during this period permitted earth observations by the two sensors, designated S193 and S194, respectively, between latitudes of  $\pm 50^\circ$ . Real-time adjustments in operating modes were made possible by communication between ground investigators and crew members on the spacecraft. The S193 sensor was a combined radiometer/scatterometer/altimeter instrument, enabling comparisons to be made between passive and active microwave responses to a variety of land and ocean surfaces [27]. The S194 sensor made coarse spatial resolution brightness temperature measurements, which have shown correlations with large-scale phenomena, such as soil moisture over the central and western portion of the U.S. [28].

The latest in the series of spaceborne surface-sensing radiometers is the Scanning Multichannel Microwave Radiometer (SMMR). This instrument was launched on both the Nimbus-7 and Seasat satellites in 1978. The instrument has been described in detail by Gloersen and Barath [29], and Njoku *et al.* [30]. The additional capabilities of the SMMR over previous radiometers are primarily in the measurement of sea-surface temperature and wind speed. However, the five-frequency dual-polarization instrument also measures atmospheric water vapor,

liquid water and rain rate, sea-ice concentration, ice type, snow cover, and can provide information on soil moisture. The effect of surface temperature on the emissivity and brightness temperature of the ocean is well understood [31], [32]. Wind speed, however, affects the surface emissivity only indirectly through the generation of ocean waves and foam. The complexity of this indirect relationship has made it difficult to develop precise models of brightness temperature dependence on wind speed [33]–[36]. Techniques for inverting data from the ten brightness temperature channels to obtain the ocean and atmospheric parameters, and determinations of the accuracies of the retrieved parameters, are currently being evaluated.

The success of the Seasat oceanographic satellite mission, which operated a number of active microwave and infrared sensors in addition to the SMMR, has generated interest within NASA, NOAA, and the military for future development of operational ocean-monitoring satellites, in which passive microwave sensors will undoubtedly play a major role. Operational ice-monitoring satellites with microwave radiometers aboard can also be expected to receive impetus in the years ahead. The outlook for operational spaceborne radiometers in earth resources and land applications is less clear. Although spacecraft radiometer experiments for the land applications will most likely be continued in the coming years, much research and experimental analysis remain to be done to understand the complex terrain electromagnetic interactions before the microwave data can become of operational use.

### III. SPACEBORNE RADIOMETER SYSTEM CONCEPTS

Spaceborne radiometer systems may have a variety of characteristics related to their specific applications. However, there are certain basic features common to most systems which can be broadly classified into radiometer system features and features related to the spacecraft platform. These general features will be discussed here, prior to a more detailed discussion of individual sensors in the next section.

#### A. Radiometer System Description

Radiometer systems for microwave remote sensing typically consist of three basic subsystems: 1) an antenna and scan subsystem, which receives incoming radiation from specified beam-pointing directions; 2) a radiometer receiver and electronics subsystem, which detects and amplifies the received radiation within a specified frequency band; and 3) a data and control subsystem, which provides timing and sequencing signals for the antenna and radiometer subsystems, and performs digitizing, multiplexing, and formatting functions on the radiometric and housekeeping data to form the output digital data stream. In spaceborne applications, the microwave radiometer may be only one of a number of different sensor types on the spacecraft. Thus the radiometer output is typically interfaced with data from the other sensors and transmitted to ground via the spacecraft data system. On the ground, data from each sensor are separated and combined with ancillary spacecraft data such as ephemeris and timing data to form the basic sensor data record. For the microwave radiometer, the sensor data record forms the input to three stages of data processing: 1) radiometer calibrations, in which the radiometer digital output voltages are converted into units of antenna temperature; 2) antenna pattern corrections, in which effects of radiation entering the antenna sidelobes are accounted for; and 3) geophysical parameter retrievals, in which brightness temperatures measured by the radiometer system are interpreted in terms of the corre-

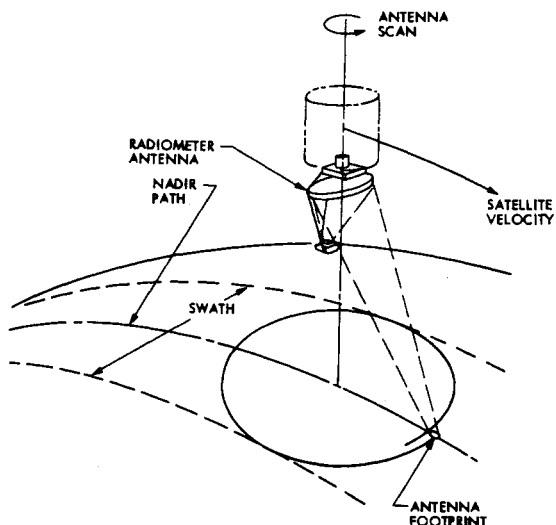


Fig. 3. Conical scan configuration, illustrating constant earth-incidence angle feature over wide swath.

sponding surface or atmospheric features. Stages 1) and 2) are usually considered as instrument-related stages in the data processing, with brightness temperatures as the final processed sensor outputs, whereas stage 3) involves modeling of the surface and atmospheric emission characteristics and the use of various data-inversion techniques. For some applications, not all of these data-processing steps are necessary. For example, brightness temperature images of the polar regions are sufficient to show the variations in extent and type of sea ice, by virtue of the large brightness temperature contrasts between ice and water and between the different ice types.

To provide global coverage with adequate spatial resolution from earth-viewing remote sensors in orbit, scanning antennas are required. Microwave antennas may be scanned either mechanically as in rotating reflectors, or electrically as in phased-array antennas. Whichever type is used, scanning is generally in the cross-track dimension, and coverage in the other dimension is provided by the spacecraft motion (the situation is somewhat different at geosynchronous altitude, where the spacecraft remains fixed over a given point on the earth). One particular scan geometry which has become popular for both scanned reflector antennas and phased arrays is the conical scan, in which the beam is offset at a fixed angle from nadir and scanned about the vertical (nadir) axis. The beam thus sweeps out the surface of a cone. This is illustrated by the diagram in Fig. 3. If the full  $360^\circ$  of a scan is utilized, double coverage fore and aft of the spacecraft is obtained. The main advantage of this type of scan is that the angle of incidence of the antenna beam at the earth's surface is constant, independent of scan position. This significantly increases the accuracy with which the brightness temperature data can be interpreted in terms of surface parameters.

For spaceborne applications, most experience to date has been achieved using radiometers of the Dicke-switched superheterodyne type. An example of this type of system is shown in Fig. 4. Prior to the receiver portion of the radiometer is a network of switches. The first of these determines which of a number of signals are to be fed into the receiver, either a signal from the vertical or horizontal antenna ports, or from one of the two calibration targets. Measurements of the calibration targets are used later in the data processing to calibrate the radiation received via the antenna in units of antenna temperature. The Dicke switch switches periodically at a high rate be-

tween the incoming signal and a known reference source. A synchronous detector at the other end of the receiver demodulates the signal. By these high-frequency comparisons of the signal with a known reference source, the effect of low-frequency gain variations in the amplifiers and other active devices is minimized. The local oscillator (LO) frequency is at the center of the desired radiometer passband and is mixed with the input signal to produce an intermediate-frequency (IF) signal which is then amplified and detected. In this system, the critical noise component is the mixer, and considerable effort is made to keep this as low noise as possible to improve the receiver sensitivity. After demodulation, the signal is integrated and sampled, and output to the data system. The critical receiver parameters in determining the temperature sensitivity ( $\Delta T_{\text{rms}}$ ) of the radiometer are the receiver noise temperature  $T_R$ , the receiver predetection bandwidth  $B$ , and the integration time  $\tau$ . For a Dicke radiometer with square-wave demodulation the sensitivity can be expressed as

$$\Delta T_{\text{rms}} = \frac{2(T_A + T_R)}{\sqrt{B\tau}}$$

where  $T_A$  is the antenna temperature [37]. As available integration time becomes smaller in advanced systems designed for high surface spatial resolution, total-power radiometers can be considered. Total-power radiometers are simpler in concept since they have no Dicke switch and demodulator. This results in approximately a factor-of-two improvement in sensitivity. The disadvantage is that variations in output level caused by changes in gain and bandwidth of the amplifiers are not compensated for. Recent advances, however, in component technology and circuit design have improved stability to the point where total-power radiometers are now being implemented in designs for future satellite radiometer systems [38]. The development of low-noise RF amplifiers may in the future also eliminate the requirements for LO/mixer heterodyne systems at the lower microwave frequencies, thus resulting in a reduction in receiver noise temperature. Other radiometer systems than described above have also been used in the past for various applications with varying degrees of success [39].

The instrument data processing usually occurs in the ground segment and consists of data calibrations and antenna pattern corrections. The data are calibrated using an equation which converts radiometer output voltage levels to antenna temperatures referenced to the antenna input ports. This equation makes use of radiometric data from the two radiometer calibration targets of known microwave temperature. The form of the equation is derived from prelaunch instrument calibration in a thermal-vacuum chamber which simulates space conditions. The equation is essentially linear, but nonlinearities in instrument performance over the range of operating conditions may require nonlinear terms to be added to the calibration equation. The calibrated data must also be corrected for effects due to the antenna. The antenna receives radiation from regions of space defined by the antenna pattern. The antenna pattern is usually strongly peaked along its beam axis, and when pointing at the ground its spatial resolution or footprint is generally defined by the angular region over which the antenna power pattern is less than 3 dB down from its value at beam center. Contributions to the antenna temperature from regions outside the footprint region are accounted for by inversion of the antenna pattern equation. This inversion procedure rapidly becomes complex as increasing accuracy is sought in deriving brightness temperatures for the 3-dB footprints. A tradeoff usually occurs between data-processing complexity and bright-

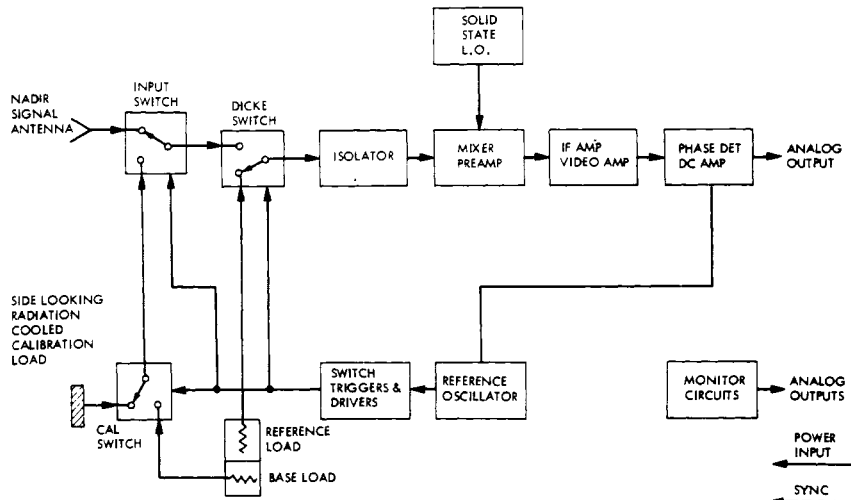


Fig. 4. Typical Dicke-switched superheterodyne radiometer configuration as implemented in NEMS (Nimbus-5).

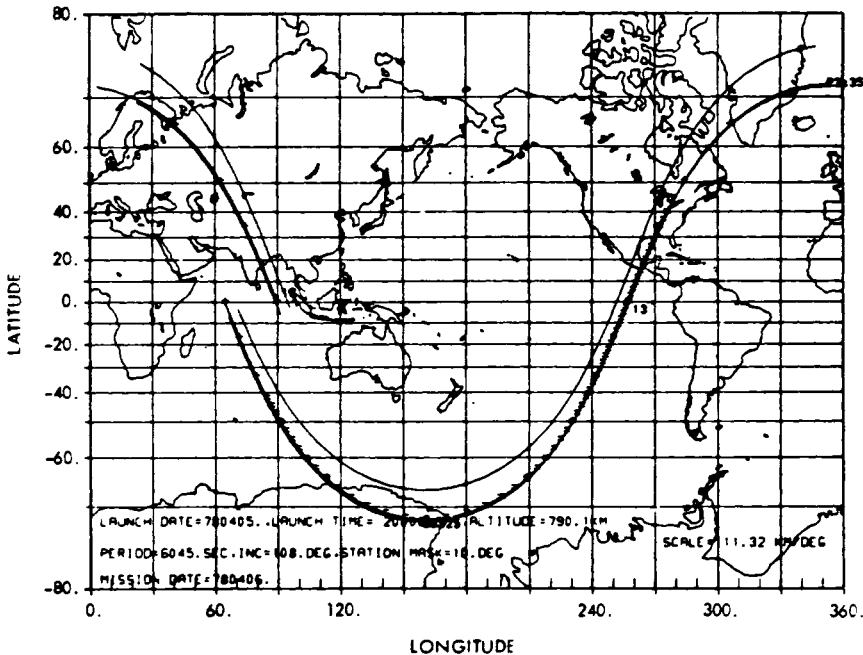


Fig. 5. Mercator projection of Seasat SMMR swath coverage for a single orbit. Asymmetry is due to offset scan.

ness temperature accuracy. The situation can be improved considerably by the design of antennas with high beam efficiency and low sidelobes.

The remaining data processing consists of interpreting the brightness temperatures in terms of the desired geophysical variables. This involves physical models of microwave emission from the earth's atmosphere and surface and the use of various data inversion techniques. Since these techniques depend on the particular application, further discussion will be delayed until the description of specific spacecraft sensors in the next section.

#### B. Spacecraft Considerations

Microwave radiometers are typically one of several sensors flown together on a spacecraft to form a combined remote-sensing payload. Besides being a platform used to place the microwave radiometer system in orbit, certain aspects of the

spacecraft or satellite mission design can influence the utility of the radiometer data. These are 1) orbit design, 2) attitude control, and 3) the data processing and transmission network.

For the nongeosynchronous, circular earth orbits most commonly used in microwave remote sensing, the orbital parameters of importance are altitude, inclination, and the related ground trace pattern. The orbital altitude and the sensor scan geometry together determine the swath width on the earth's surface. The orbit inclination determines the latitude range of coverage. The altitude and inclination together determine the nodal precession rate and the ground trace pattern. As an example, Fig. 5 shows a Mercator projection of the Seasat SMMR swath coverage for a single orbit. The Seasat orbit was approximately circular, with an altitude of 800 km, inclination of 108°, and period of 101 min. The orbit was chosen as a compromise between the requirements of the various active and passive sensors on the spacecraft. For further discussion of orbit considerations see King [40]. The spacecraft attitude (i.e., stability in

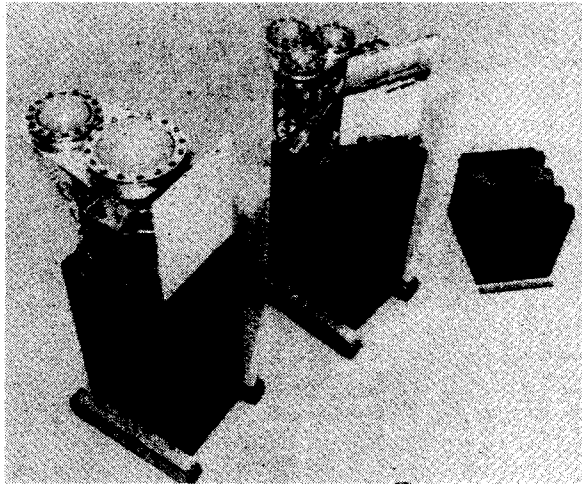


Fig. 6. Photograph of NEMS instrument (Nimbus-5) showing separate  $\text{H}_2\text{O}$  and  $\text{O}_2$  modules and power supply module.

orbit) is also an important factor for remote sensors. Spacecraft attitude is normally described by three angles in a rectangular coordinate system: pitch, roll, and yaw. Deviations of these angles from their nominal values are referred to as attitude errors and affect a radiometer system in three ways: 1) error in footprint location at the earth's surface; 2) rotation of antenna polarization vectors relative to polarization defined at the surface; and 3) deviation of antenna beam incidence angles at the earth's surface from their nominal value. Each of these three effects can give rise to errors in interpretation of the radiometric data. Spacecraft attitude is normally controlled within specified tolerances by the use of attitude sensors and compensatory mechanisms.

#### IV. SPACEBORNE RADIOMETRIC SENSORS

In this section the key experimental radiometric sensors and the scientific results obtained from their data will be discussed. The discussion emphasizes those sensors flown on the spacecraft listed in Table II. Operational sensors are referred to in the next section.

##### A. NEMS (Nimbus-5)

The Nimbus-5 Microwave Spectrometer (NEMS) was the first microwave temperature sounder flown in space [41]. The instrument could be considered as composed of two parts: 1) three channels at center frequencies 53.65, 54.9, and 58.8 GHz for measuring primarily the atmospheric temperature profile; 2) two channels at 22.234 and 31.4 GHz, sensitive over the oceans to water vapor and liquid water, and indicating emissivity and surface temperature over land. Although these two parts could operate separately, performance was improved by using data from all channels simultaneously in the profile and parameter estimations. A photograph of the NEMS instrument is shown in Fig. 6. The instrument comprised four main functional units as shown in the functional block diagram (Fig. 7). These were: 1) the  $\text{H}_2\text{O}$  radiometer unit, 2) the  $\text{O}_2$  radiometer unit, 3) the data/programmer unit, and 4) the power supply unit.

The  $\text{H}_2\text{O}$  radiometer unit consisted of channels  $R_1$  (22.235 GHz) and  $R_2$  (31.4 GHz), which were completely independent. Each was fed by a lens-loaded circular horn, nadir-viewing, with a 3-dB beamwidth of  $10^\circ$ . This provided a surface footprint of about 190-km diameter. The  $\text{O}_2$  radiometer unit consisted of channels  $R_3$ ,  $R_4$ , and  $R_5$  (53.65, 54.9, and 58.8 GHz),

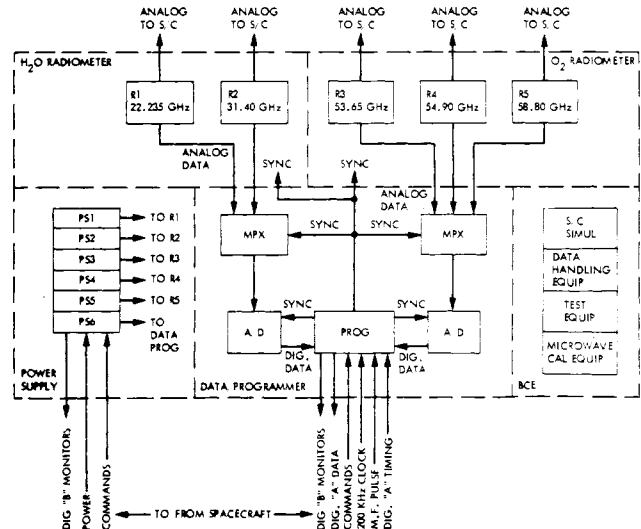


Fig. 7. NEMS (Nimbus-5) functional block diagram.

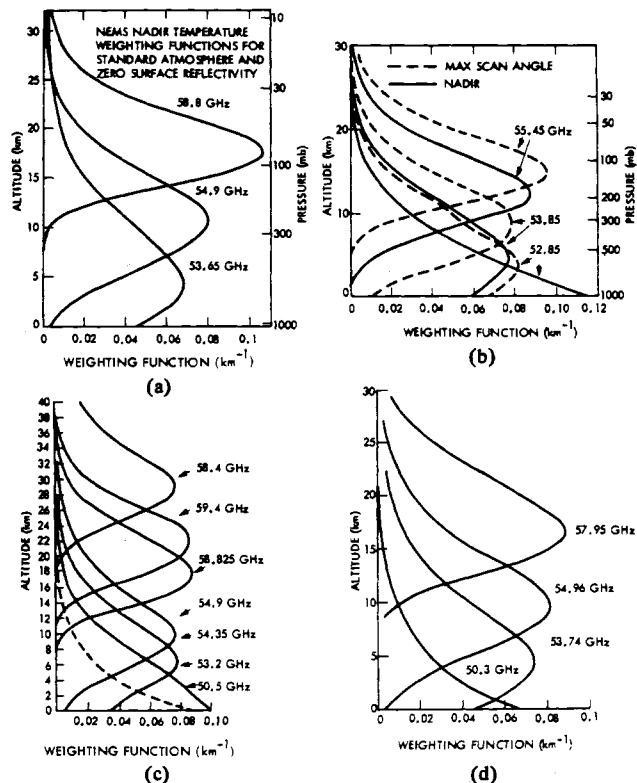


Fig. 8. Atmospheric temperature weighting functions viewing earth from space: (a) NEMS (Nimbus-5); (b) SCAMS (Nimbus-6); (c) SSM/T (Block-5); (d) MSU (Tiros-N). Calculations assumed a calm sea background for (b), (c), and (d), and zero surface reflectivity for (a).

which were also independently operating radiometers. The five radiometer channels were functionally identical and of the Dicke-switched, superheterodyne type, with two-point calibration system as shown in Fig. 4.

The NEMS channels 3, 4, and 5 atmospheric temperature weighting functions are shown in Fig. 8(a). These enabled atmospheric temperature to be sensed in the troposphere and lower stratosphere. To determine the atmospheric temperature profile at a number of discrete points using data from the three

**TABLE II**  
**U.S. EARTH-ORBITING SPACECRAFT WITH EXPERIMENTAL  
 PASSIVE MICROWAVE SENSORS**

Satellite Characteristics	Nimbus-5	Skylab Earth Resources Experimental Package (EREP)	Nimbus-6	Seasat	Nimbus-7
Launch date	December, 1972	May, 1973	June, 1975	June, 1978	October, 1978
Main Program Objectives	Development of measurement techniques for atmospheric processes related to meteorology and general circulation.	Development of visible, infrared, and microwave sensors, and data evaluation techniques for Earth resource applications from space.	To sound the atmosphere using advanced techniques extending measurement capabilities demonstrated on previous Nimbus satellites.	Proof-of-concept mission to demonstrate: (1) techniques for global monitoring of oceanographic phenomena; (2) key features of an operational ocean monitoring system.	To conduct experiments in the pollution, oceanographic and meteorological disciplines. Refine atmospheric measurement capabilities demonstrated on previous Nimbus satellites.
Sensor Payload	Temperature Humidity Infrared Radiometer Surface Composition Mapping Radiometer (SCMR) Electrically Scanning Microwave Radiometer (ESMR) Infrared Temperature Profile Radiometer (ITPR) Selective Chopper Radiometer (SCR) Nimbus-E Microwave Spectrometer (NEMS)	Multispectral Photographic Cameras (S190A) Earth Terrain Camera (S190B) Infrared Spectrometer (S191) Multispectral Scanner (S192) Microwave Radiometer / Scatterometer and Altimeter (S193) L-band Radiometer (S194)	THIR ESMR High Resolution Infrared Radiometer Sounder (HIRS) Scanning Microwave Spectrometer (SCAMS) Earth Radiation Budget (ERB) Limb Radiance Inversion Radiometer (LRIR) Pressure Modulator Radiometer (PMR)	Radar Altimeter (ALT) Seasat-A Satellite Scatterometer (SASS) Synthetic Aperture Radar (SAR) Scanning Multi-channel Microwave Radiometer (SMMR) Visible and Infrared Radiometer (VIRR)	THIR SMMR ERB Coastal Zone Color Scanner (CZCS) Limb Infrared Monitor of the Stratosphere (LIMS) Stratospheric Aerosol Measurement (SAM II) Stratospheric and Mesospheric Sounder (SAMS) Solar Backscatter Ultraviolet and Total Ozone Mapping Spectrometer (SBUV/TOMS)
Orbit Characteristics:					
Altitude	Circular sun-synchronous 1100 km	Circular sun-synchronous 1100 km	800 km	Circular	±0.7°
Inclination	99°	50°	108°	955 km	±1.0°
Attitude Stabilization:	+1.0° +0.5° +0.5°	+2.0° +2.0° +2.0°	±0.5° ±0.5° ±1.0°	99.2°	±1.0°

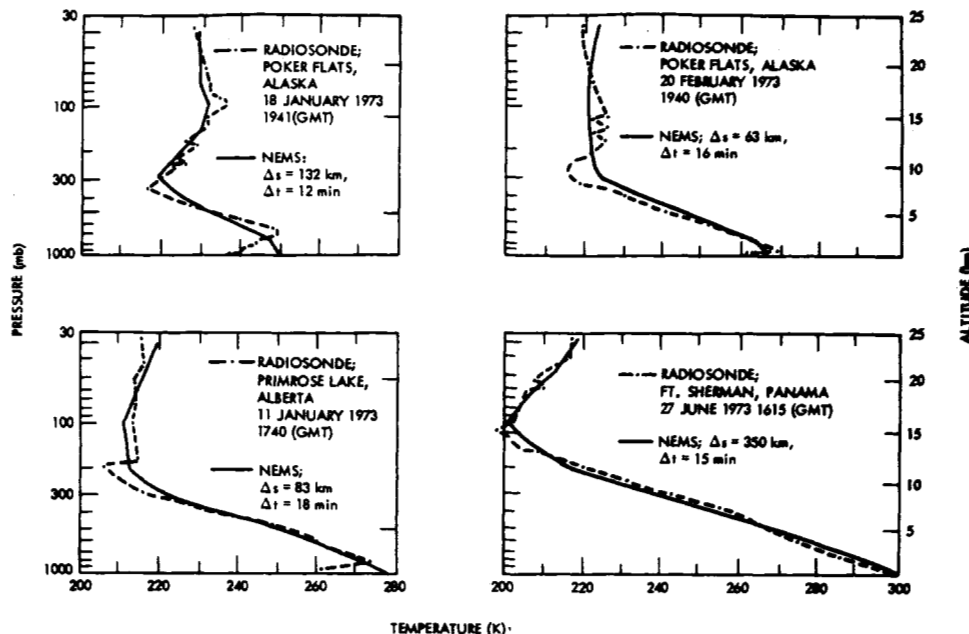


Fig. 9. Comparisons of individual temperature soundings by NEMS and coincident radiosondes. The spatial difference  $\Delta s$  and time difference  $\Delta t$  of the NEMS sounding relative to the radiosonde are indicated for each sounding (after Waters *et al.* [11]).

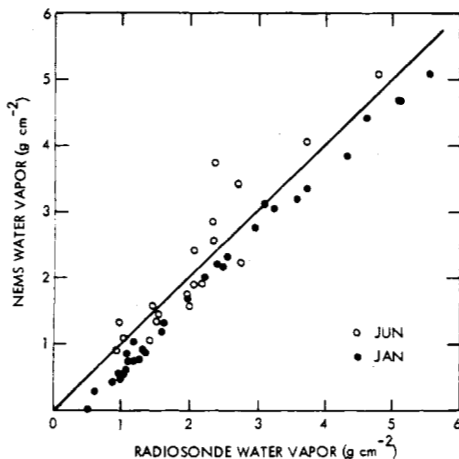


Fig. 10. Comparisons of NEMS water vapor retrievals with radiosonde water vapor measurements (after Staelin *et al.* [13]).

brightness temperature channels, a statistical retrieval approach was used, incorporating *a priori* statistics from radiosonde data and atmospheric model calculations. Results from NEMS using this approach are illustrated in Fig. 9. These show the NEMS-retrieved profiles compared with radiosonde data in four different situations. The errors are largest where sharp changes in profile occur, showing the limitations in vertical resolution imposed by the width of the weighting functions. Comparisons using the most reliable NMC temperature profiles indicated that the NEMS rms temperature accuracy averaged over the profile was about  $2^{\circ}\text{C}$ . The effects of clouds on the profile retrieval accuracy were investigated by Staelin *et al.* [12]. Clouds were observed to affect less than 0.5 percent of the temperature profile soundings. Most such effects occurred in the intertropical convergence zone (ITCZ) and altered the inferred temperature profile by less than a few degrees centigrade. Furthermore, these large clouds could be detected by NEMS channels 1 and 2 and thus could be accounted for in applications of the data.

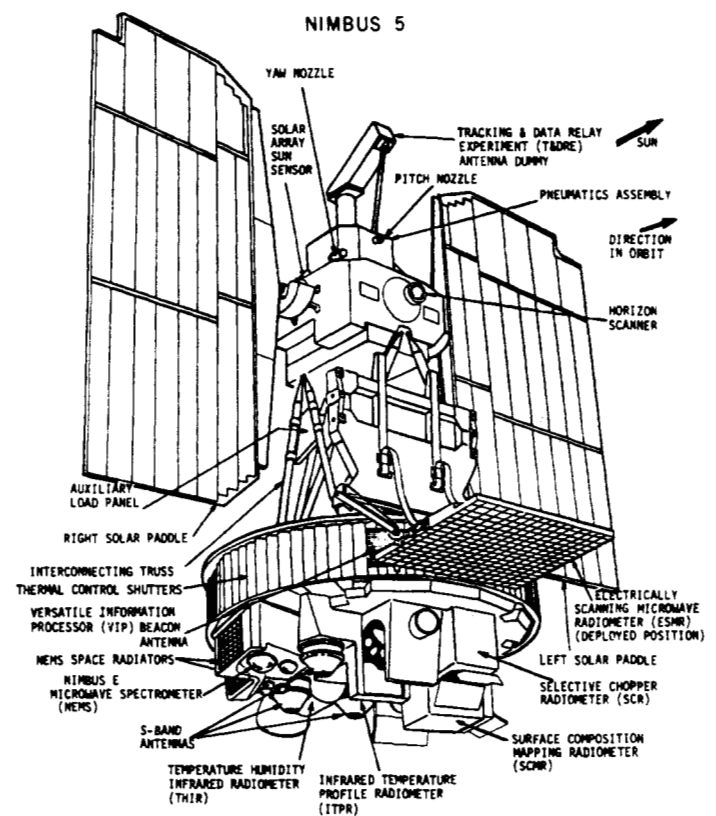


Fig. 11. Nimbus-5 satellite, launched December 1972, showing placement of NEMS and ESMR sensors.

The NEMS channels 1 and 2 were used for determining columnar atmospheric water vapor and liquid water abundances using simple regression approaches [13], [42]. The accuracy of NEMS water vapor estimates was tested by comparison with radiosondes launched from ships and islands. The results are shown in Fig. 10 and indicate an overall rms accuracy of about

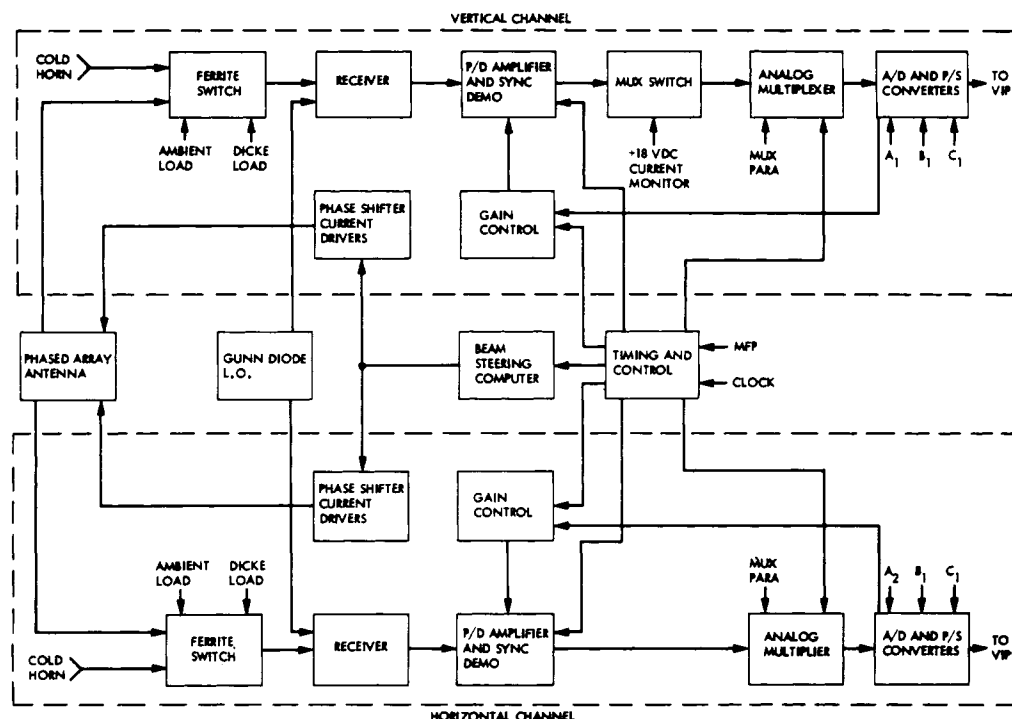


Fig. 12. System block diagram of ESMR (Nimbus-6).

0.4 g/cm<sup>2</sup>. Accuracy for the NEMS liquid water estimates was difficult to determine experimentally since there were no reliable sources of comparison data. Theoretical rms accuracies were estimated as 0.01 g/cm<sup>2</sup>.

Whereas NEMS channels 1 and 2 could be used for atmospheric water determinations over the oceans, they also provided information on the global distribution and character of various types of snow and ice. Seasonal variations in the ice and snow, and different types of sea ice and firn, could clearly be distinguished from observations in the polar regions [23].

#### B. ESMR (Nimbus-5)

The Electrically Scanning Microwave Radiometer (ESMR) was first launched aboard the Nimbus-5 satellite in December 1972. Its objective was to map surface features of the earth by means of received radiation at 19.35 GHz, particularly the distribution of polar ice and precipitating clouds over ocean areas [43].

The instrument consisted of four major components: 1) a phased-array microwave antenna consisting of 103 waveguide elements each having its associated electrical phase shifters; 2) a beam-steering computer which determined the coil current for each of the phase shifters for each beam position; 3) a microwave receiver with center frequency 19.35 GHz; and 4) timing control and power circuits. The instrument is shown diagrammatically on the Nimbus-5 spacecraft in Fig. 11. The block diagram is similar to one channel of the ESMR on Nimbus-6 (shown in Fig. 12). The radiometer was of the Dicke-switched superheterodyne type.

The aperture area of the phased-array antenna was 83.3 X 85.5 cm, with polarization linear and parallel to the spacecraft velocity vector. The antenna beam was scanned cross-track (i.e., perpendicular to the spacecraft velocity vector) in 78 steps, ±50° from nadir, every 4 s. Scanning was achieved by means of the electric phase shifters in series with each waveguide element and controlled by timing commands via a beam-steering

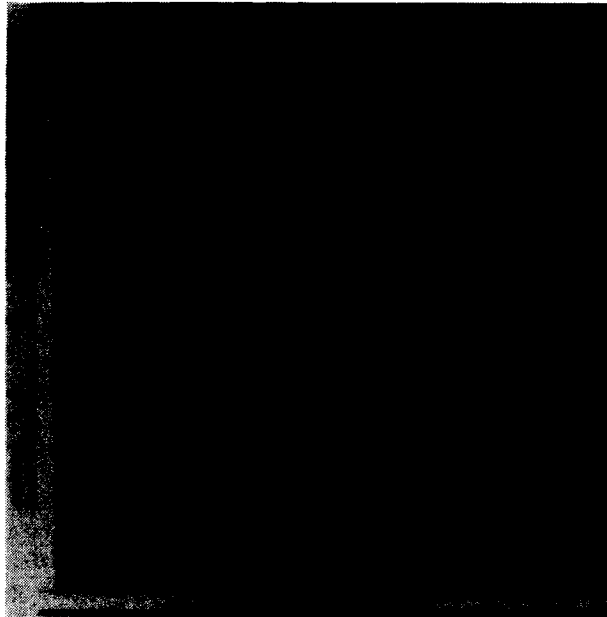
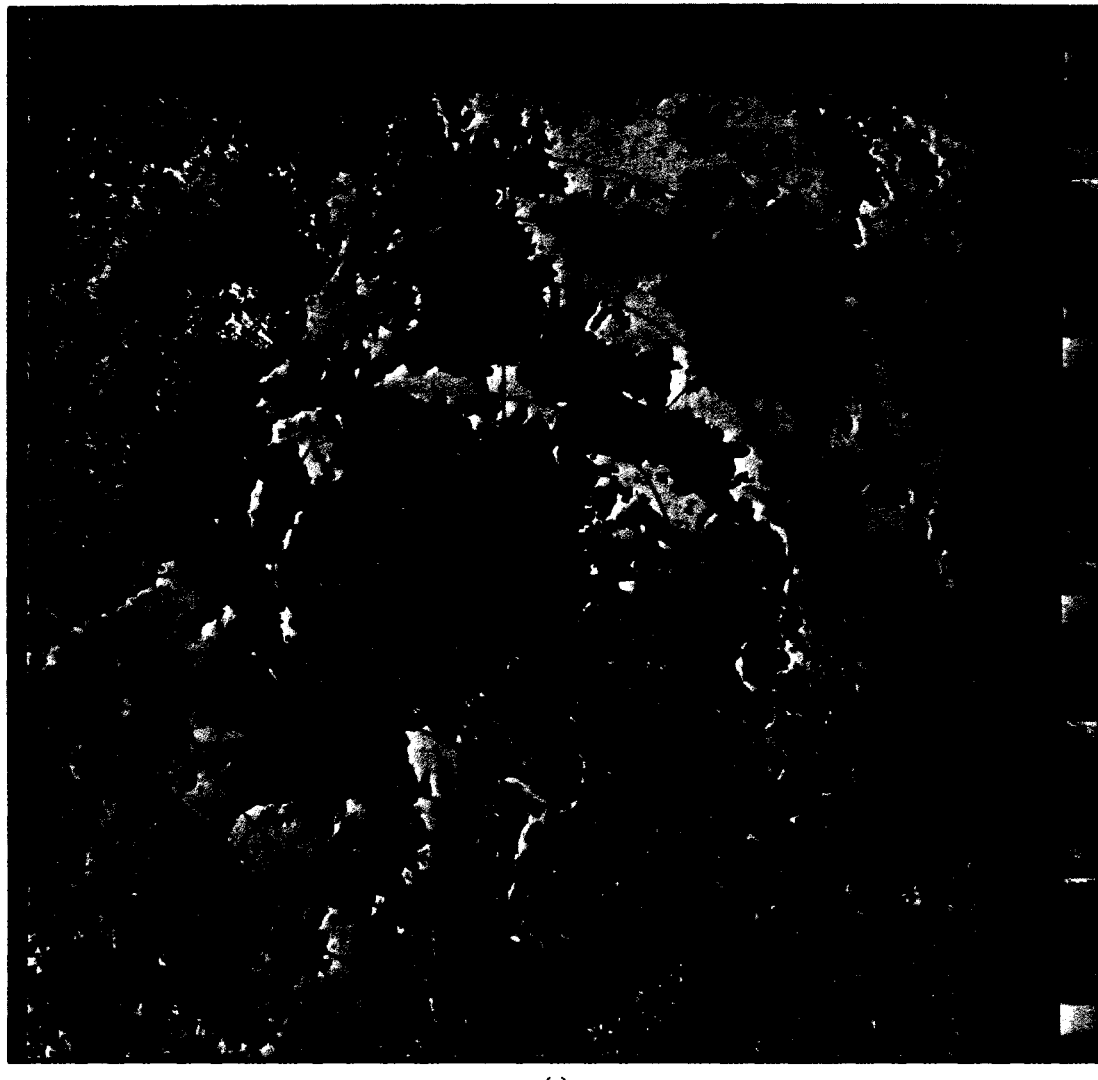


Fig. 13. Photograph of ESMR waveguide phased array antenna.

network. A photograph of waveguide array is shown in Fig. 13. The antenna beamwidth was 1.4° X 1.4° near nadir, and degraded to 2.2° crosstrack X 1.4° down-track at the 50° scan extremes. From a nominal orbit of 1100-km altitude the footprint resolution was 25 X 25 km near nadir, degrading to 160 X 45 km at the ends of scan. The swath width generated by the ±50° cross-track scan was 1570 km, with overlap extending to the equator crossings for successive orbits. Thus complete global coverage, including the polar regions, was obtained within 12 h, counting both day and night portions of the orbit. To account for effects of antenna sidelobes a simple one-dimensional correction was applied to the antenna temperatures. This was sufficient due to the low antenna sidelobe levels in the plane



(a)

Fig. 14. Images of north polar region generated from brightness temperatures measured by the Nimbus-5 ESMR: (a) winter (January 1973) (after Zwally and Gloersen [24]).

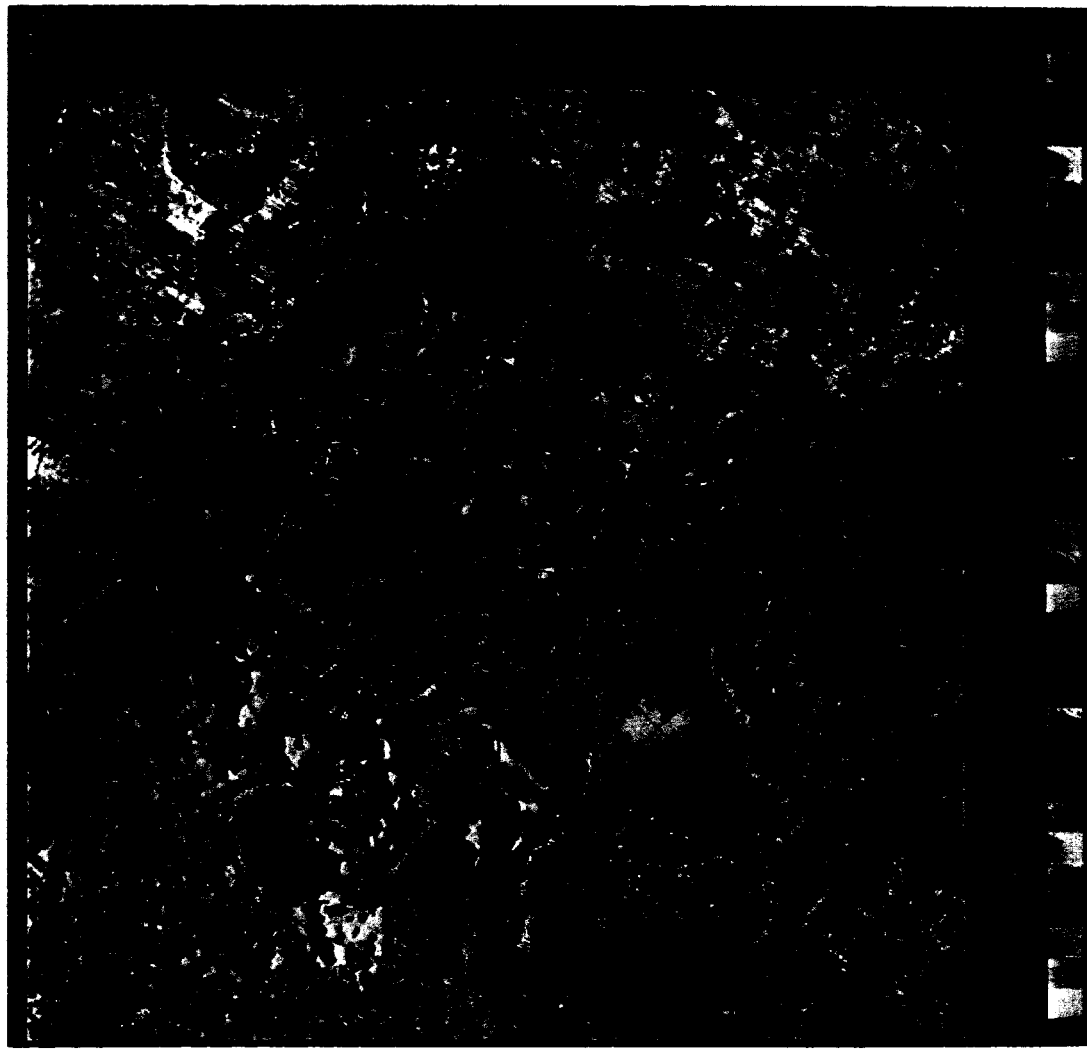
parallel to the waveguide elements. A matrix operation on the 78 antenna temperatures in each scan performed the necessary corrections for each beam position.

The ESMR capability for providing images of the polar ice-caps, through clouds, and both day and night, has found important applications in polar research and marine operations. There is a large contrast in brightness temperature between open sea water and completely consolidated sea ice. Thus intermediate brightness temperatures occurring within the ~35-km ESMR footprint could be ascribed to mixtures of open water and ice, whose percentage concentrations could be estimated to an accuracy of about 15 percentage points. This accuracy is affected to some extent by the existence of three radiometrically distinct sea ice types: first year, multiyear, and first year thin sea ice. These ice types each have characteristic emissivities due to their surface and internal structure. Fig. 14 shows two ESMR images of the arctic at different seasons. The winter (January 15, 1973) image shows the ice canopy to be composed of two general types of ice: the principally multiyear ice covering the main portion of the Arctic Ocean, with brightness temperatures ranging from 209 to 223 K, and either first-year or first-year/multiyear mixtures with higher brightness temperatures covering the southern portions of the marginal seas. By the end of the

summer melt season, the ESMR image for the late summer (September 9, 1973) shows that most of the ice that covered the marginal seas has melted. Detailed examination of year-round images such as these has provided a wealth of information on the complex morphology and dynamics in the artic and antarctic regions [24], [44]–[47].

Over the oceans the ESMR has been shown to be capable of detecting precipitation areas. These appear in the ESMR images as regions of high brightness temperature caused by the larger droplet sizes and total water content in precipitating clouds [26]. Meteorological applications of these images compared to images from infrared and visible sensors have been discussed by Wilheit *et al.* [25]. Similar studies by Allison *et al.* [48] and Adler and Rodgers [49] have used the ESMR data to provide semi-quantitative rainfall characteristics of oceanic tropical cyclones and to study convergence phenomena in regions not often detectable with other satellite sensors.

ESMR measurements have also been shown to be responsive to soil-moisture conditions over large land areas [50]. At the ESMR frequency (19.35 GHz), correlations with soil moisture are limited to predominantly bare soil and low vegetation density areas. Because of this limitation, and the relatively coarse spatial resolution, current applications of this



(b)

Fig. 14. Images of north polar region generated from brightness temperatures measured by the Nimbus-5 ESMR: (b) summer (September 1973) (after Zwally and Gloersen [24]).

kind of data are limited. These studies do indicate future potential, however, for instruments designed specifically for soil-moisture applications.

#### C. S-193 (*Skylab*)

The *Skylab* microwave radiometer/scatterometer and altimeter instrument, designated S-193, was one of six experimental remote sensors making up the Earth Resources Experimental Package (EREP), operated on *Skylab* missions between May 1973 and February 1974. The three instrument components operated at the same frequency (13.9 GHz) and shared a common antenna and scan system. Certain electronic subsystems were also shared to minimize weight and power requirements. The instrument objectives were to make simultaneous measurements of radar backscatter and radiometric brightness temperature from orbit, in a number of scanning modes, primarily for the purpose of studying winds and precipitation over the oceans. The instrument has been described by Potter *et al.* [51] and Moore *et al.* [52], and is shown on the spacecraft in Fig. 15.

The (S-193) antenna was a 115-cm-diameter mechanically scanned parabolic reflector, with dual polarization and a 2°

beamwidth. The antenna was gimballed, permitting antenna scanning both along and across the flight path, and at the nadir position provided a circular footprint of 16-km diameter. Drive commands were received from an antenna controller which could follow any of four preset scan modes. A block diagram of the system is shown in Fig. 16. The signal from the antenna was preamplified using a tunnel-diode amplifier, and the IF signal generated by the mixer was split between the radiometer and scatterometer receivers. After detection and integration, the output was digitized and recorded on an EREP 10-kbit/s tape-recorder channel. The calibration source box contained two calibration sources, used for temperature reference and to set the automatic gain control of the radiometer receiver. Three choices of receiver integration times were available in an effort to accommodate the different scan modes of the antenna. Complete calibration of the system including the antenna was not performed prior to launch. Instead, the antenna insertion loss and the system transfer function were computed in orbit, based on measurements with the antenna pointed towards cold space or assumed microwave temperature 2.7 K.

Analysis of the radiometric data was directed towards studying correlations between the active and passive data over a variety of surface types. These correlations were studied using



Fig. 15. Skylab, launched May 1973, showing location of EREP sensors on the multiple docking adaptor.

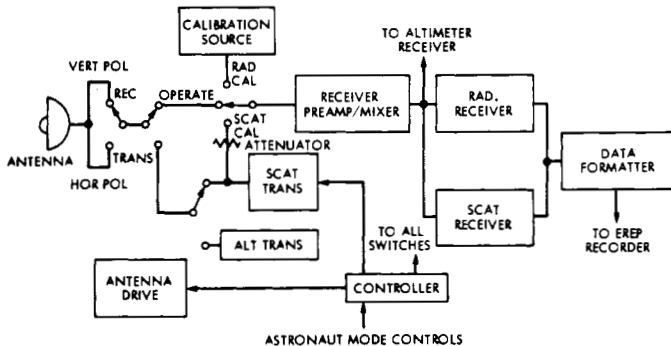


Fig. 16. Skylab S-193 system block diagram.

data measured at antenna scan angles between  $0^\circ$  and  $48^\circ$  from nadir. Lowest correlations were found between active and passive data at vertical polarization and  $30^\circ$  nadir angle [27]. Effects of clouds and weather, however, probably significantly affected the results, making conclusions about surface effects difficult. Studies of the effects of soil moisture on the radiometer response were reported by Moore *et al.* [53]. Since soil-moisture surface measurements were difficult to obtain, a related antecedent precipitation index (API) was used instead. Although a trend was evident towards lower emissivities with higher API, the correlation was relatively low, probably due to the many assumptions in the API model and the significant effects of surface roughness and vegetation at 13.9 GHz. Another study by Ulaby *et al.* [54] compared data from the S-193, S-194 (1.4-GHz), and ESMR (19.35-GHz) sensors, over the Utah Great Salt Lake Desert. Within this region, large decreases in brightness temperature and increases in backscattering coef-

ficients were observed, as a result of the smooth, bare nature of the surface and possible effects of subsurface brine sediments. Results from the scatterometer portion of the instrument are discussed in more detail by Moore and Young [55].

#### D. S-194 (Skylab)

The S-194 was an *L*-band (1.4-GHz) radiometer system flown as part of the EREP remote-sensing payload on Skylab. The objective was to measure radiation from the earth at this frequency, with application to earth resources and in particular soil moisture. The instrument consisted of a fixed, nadir-viewing, phased-array antenna, and receiver, calibration, and data subsystems [51]. The antenna beamwidth was  $15^\circ$ , providing a surface footprint of 115-km diameter. The radiometer was a modified Dicke type, with tuned RF receiver and gain modulation. The instrument is shown on the spacecraft in Fig. 15.

In addition to comparisons with S-193 and ESMR data (described above), the data from S-194 were studied for correlations with soil moisture by Eagleman and Lin [28]. Due to the large footprint size, water balance models were used to extrapolate point measurements of surface soil moisture for comparison with the spacecraft data, Fig. 17. The observed correlations with soil moisture in the top 2.5 cm were quite high. However, the data points used were not strictly independent since they represented footprints with significant amounts of overlap. Studies by McFarland [55] using the antecedent precipitation index showed similar results.

#### E. SCAMS (Nimbus-6)

The Scanning Microwave Spectrometer (SCAMS) on Nimbus-6 had similar objectives to the NEMS instrument, i.e., to deter-

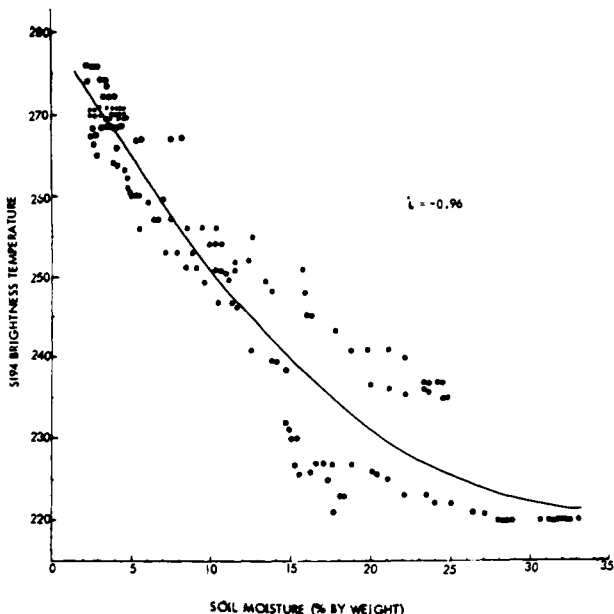


Fig. 17. Skylab S-194 brightness temperature relationship with soil moisture over Kansas and Texas sites, 1973 (after Eagleman and Lin [28]).

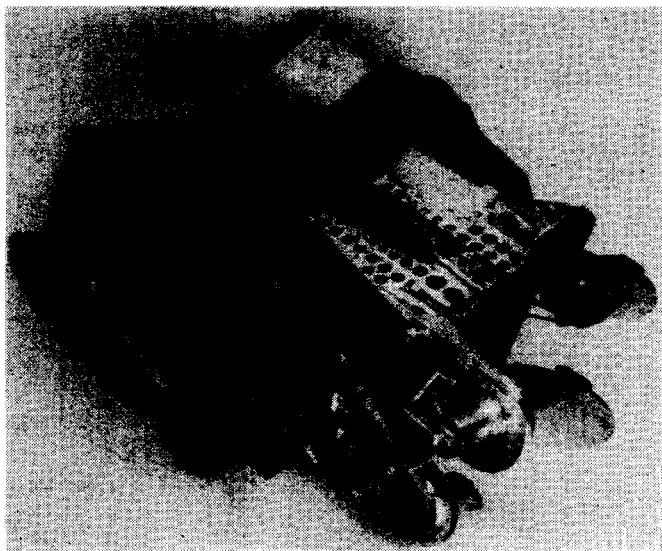


Fig. 18. Photograph of SCAMS instrument (Nimbus-6).

mine atmospheric temperature profiles and, over ocean surfaces, the abundances of water vapor and liquid water in the atmosphere [57]. Whereas NEMS observed atmospheric parameters at nadir, along the subsatellite track, SCAMS operated by scanning to either side of this track to produce maps of these parameters with nearly full earth coverage. SCAMS was intended to provide a unique global data set for research and trial operational use in meteorological applications, and for use in the Global Atmospheric Research Program (GARP).

A photograph of the SCAMS instrument mounted in its assembly fixture is shown in Fig. 18. There is one antenna each for the two  $H_2O$  channels and a single antenna for the three  $O_2$  channels. Scanning was achieved by stepping a reflector in front of each antenna. Each reflector, inclined at  $45^\circ$  to its antenna, scanned the antenna beam in a left-handed sense with respect to the spacecraft velocity vector, and a complete  $360^\circ$  scan took 16 s. Thirteen earth-data samples, each separated by

a  $7.2^\circ$  scan step, were recorded between  $\pm 43.2^\circ$  from nadir. 3 s at the end of each earth scan were reserved for reflector rotation and system calibration, which took place by 1-s views of cold space and of an instrument blackbody source. The antenna beamwidths of  $7.5^\circ$  gave ground resolutions of 145 km at nadir and  $220 \times 360$  km at the edges of the scan ( $43.2^\circ$  from nadir). The  $\pm 43.2^\circ$  scan covered a swath width of 2400 km, which provided nearly full earth coverage every 12 h. The polarization vector rotated as the beam scanned. At nadir, polarization was parallel to the satellite velocity vector for all channels except channel 5 (55.45 GHz), for which it was perpendicular.

The functional operation of the SCAMS was similar to that described for the NEMS instrument. The 22.2- and 31.6-GHz channels shared no components in common, whereas the three  $O_2$  channels shared a common antenna and calibration target. A channelizing filter separated the frequencies of the two  $O_2$  channels with like polarizations; the third  $O_2$  frequency was separated by a polarization transducer. The radiometers were of the Dicke-switched superheterodyne type and, from the Dicke switchback, were identical in operation to those used on the NEMS. The use of external calibration targets viewed by the antennas was an improvement in the calibration design. By this means a more accurate system calibration was achieved for the orbital radiometric data. After calibration in the ground processing, the data were deconvolved to remove the antenna side-lobe contributions. The high beam efficiencies of the SCAMS antennas ( $\gtrsim 97$  percent) enabled this to be done fairly simply.

Weighting functions for the three temperature-sounding channels are shown in Fig. 8(b). These provided theoretical retrieval accuracies comparable to NEMS. SCAMS-derived temperatures profiles were compared with radiosonde temperatures for several European frontal systems by Grody and Pellegrino [14]. Fig. 19(a) shows a cloud image from the NOAA-4 VHRR for a case study region over Europe, with two adjacent SCAMS grid patterns for January 26 and 27, 1976. The temperature field at the 700-mbar level in the atmosphere derived from available radiosonde reports is shown in Fig. 19(b), revealing a deep trough with strong temperature gradients. Fig. 19(c) shows the 700-mbar SCAMS-derived result in which the positions of the major trough and ridge are well defined, although the amplitudes are somewhat underestimated. The rms temperature accuracies at this level for the SCAMS retrievals are about 2 K. A more stringent test of SCAMS cloud-penetrating capabilities was presented by Rosenkranz *et al.* [15], in which the instrument was used to study the development of Typhoon June over the Pacific. Results showed the possibility of deriving cloud liquid water content and sea surface winds around the typhoon from the 22- and 31-GHz channels. The 55.45-GHz channel displayed the typhoon's warm core temperature structure at the 200-mbar level. Improved spatial resolution would have increased the impact of these measurements. Kidder *et al.* [58] have also investigated the use of SCAMS data for estimation of tropical cyclone central pressure and outer winds. Fig. 20 shows SCAMS-derived columnar water vapor contours in the western Pacific, compared to local radiosonde observations. Knowledge of these large variations in water vapor within the tropical environment is of utmost importance in understanding the development of tropical cyclones and cloud clusters (see also [59]).

#### F. ESMR (Nimbus-6)

The successful operation of the ESMR on Nimbus-5 laid the basis for a second ESMR which was launched on the Nimbus-6

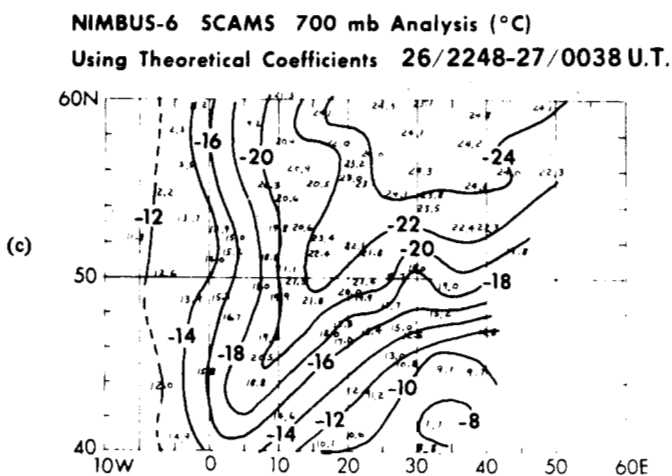
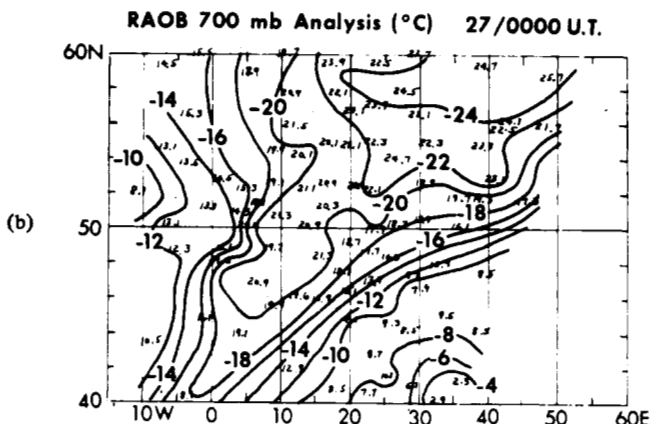
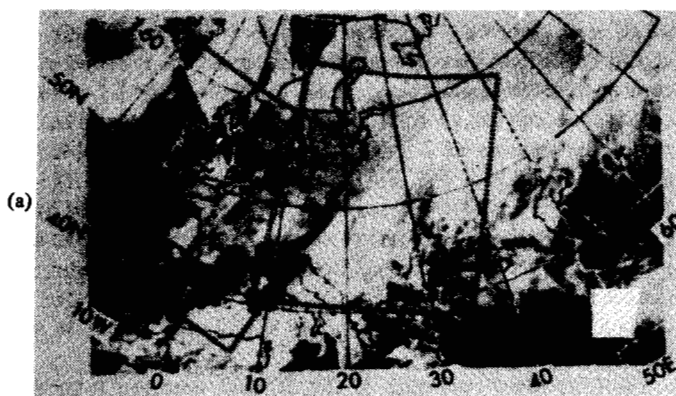


Fig. 19. Comparisons between SCAMS 700-mbar retrieved temperature measurements and radiosonde data, January 26/27, 1976: (a) NOAA-4 VHRR satellite image showing cloud features and SCAMS grid coverage; (b) analysis of 0000 UT radiosonde temperatures; (c) analysis of 2248-0038 UT SCAMS retrieved temperatures (after Grody and Pellegreno [14]).

satellite in June 1975 [60]. The operating wavelength for the Nimbus-6 ESMR (ESMR-6) was 37 GHz (as opposed to 19.35 GHz for ESMR-5). This frequency change had the effect of tripling the instrument's sensitivity to water droplets while keeping its sensitivity to water vapor essentially the same, thus making it easier to distinguish light rain areas from areas of high water vapor. A secondary effect was to roughly double the contrast between first-year and multiyear ice, although some increase in ambiguity of ice concentration determination occurred. Snowfield mapping capability was also expected to improve.

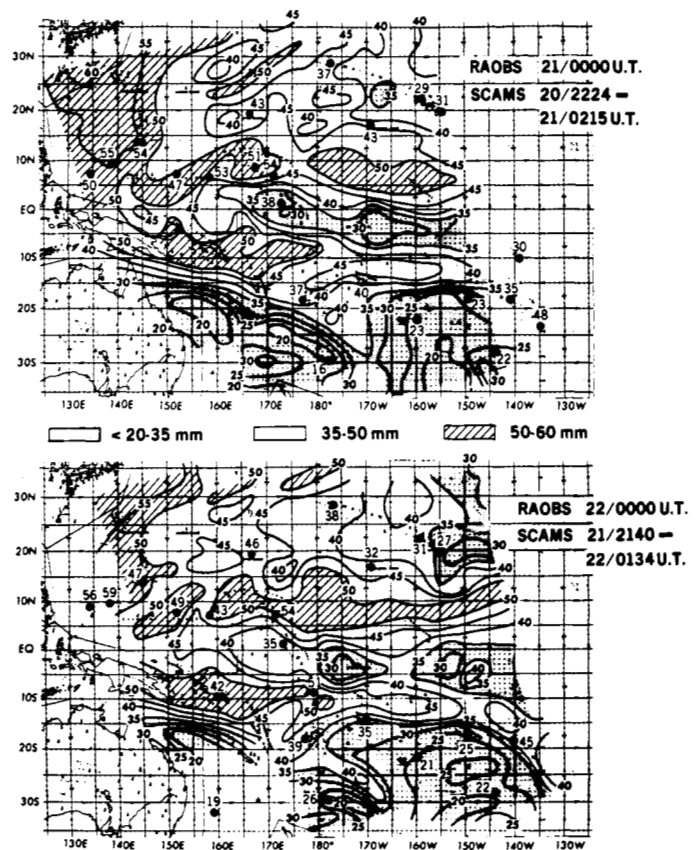


Fig. 20. Comparisons between SCAMS retrieved precipitable water (mm) and radiosonde measurements (●), August 20-22, 1975 (after Grody [10]).

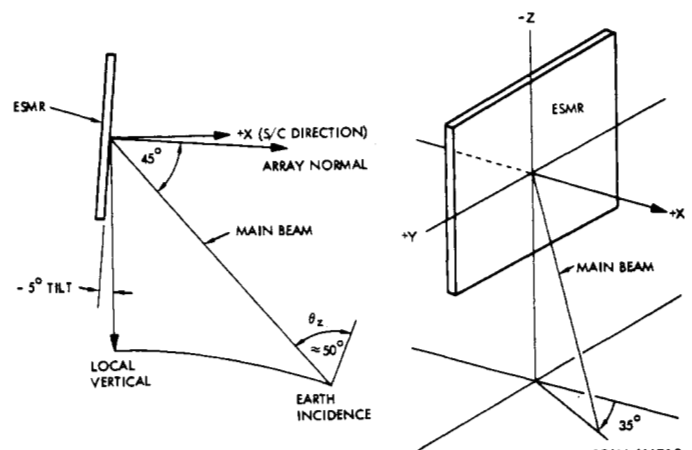


Fig. 21. ESMR (Nimbus-6) antenna scan geometry (after Wilheit [60]).

The ESMR-6 measured both horizontally and vertically polarized radiation at the 37-GHz frequency, as opposed to horizontal only for ESMR-5. The polarization information facilitated quantitative interpretation of the radiometric measurements, and provided information on winds over the oceans.

The antenna beam of the ESMR-6 scanned ahead of the spacecraft along a conical surface, with a constant angle of  $45^{\circ}$  with respect to the antenna axis (Fig. 21). The beam scanned in azimuth  $\pm 35^{\circ}$  about the forward direction in 71 steps. The 3-dB beamwidth varied from  $0.95^{\circ} \times 1.0^{\circ}$  at scan center to  $1.17^{\circ} \times 0.85^{\circ}$  at the scan extremes. The antenna axis was tipped forward  $5^{\circ}$  from the vertical axis of the spacecraft (as a design

tradeoff), which resulted in the antenna beam intersecting the earth at a nearly constant incidence angle throughout the scan. The variation of incidence angle across the scan was about  $\pm 0.6^\circ$ . The 3-dB footprint on the earth's surface had dimensions approximately 20 X 43 km. The scan pattern resulted in a swath width of 1300 km, which allowed polar coverage up to latitudes of  $85.7^\circ$ .

The radiometer section of the instrument was similar in operation to that of ESMR-5. However, there were two separate receivers, one for each polarization, with common Gunn-diode LO's (Fig. 12). Radiation of both polarizations was received and separated in the phased-array antenna before being fed into the radiometers.

The dual-polarization capability of ESMR-6 was used to study its effectiveness for improved measurements of wind speed over the ocean and rainfall rate, in addition to continuation of the polar ice studies begun with ESMR-5. Wilheit [61] analyzed coincident ESMR-6 brightness temperatures and wind measurements from NOAA data buoys to get an improved understanding of the effect of ocean emissivity on wind speed. ESMR-6 data were also used by Weinman and Guetter [62] to show the potential for using dual-polarization measurements to determine rainfall over land as well as ocean.

#### G. SMMR (*Seasat* and *Nimbus-7*)

The Scanning Multichannel Microwave Radiometer (SMMR), launched on the Seasat and Nimbus-7 satellites in 1978, is currently the state-of-the-art instrument for passive microwave surface sensing. It measures dual-polarized radiation from the earth at frequencies of 6.6, 10.7, 18, 21, and 37 GHz. The SMMR data provide information on sea surface temperature, wind speed, atmospheric water vapor, cloud and precipitating liquid water, and sea ice type and concentration. Information on soil moisture and terrain snow cover properties is also obtainable. The SMMR instrument has been described in detail by Gloersen and Barath [29], and Njoku *et al.* [30].

A front view of the SMMR is shown in Fig. 22. There are six independent Dicke-type superheterodyne radiometers, fed by a single antenna and a calibration subsystem. Fig. 23 shows the system block diagram. At 37 GHz, two radiometers simultaneously measure two orthogonally polarized components of the received signal. At the other four frequencies, the radiometers alternate between the two polarizations during successive scans. In this manner ten data channels, corresponding to five dual-polarized signals, are provided by the instrument.

The SMMR has a scanning antenna system, consisting of an offset parabolic reflector with a 79-cm-diameter collecting aperture and a multifrequency feed assembly. The antenna reflector is mechanically scanned about a vertical axis, with a sinusoidally varying velocity, over a  $\pm 25^\circ$  azimuth angle range. The antenna beam is offset  $42^\circ$  from nadir, thus the beam sweeps out the surface of a cone and provides a constant incidence angle at the earth's surface. Calibration is achieved by alternately switching in a "cold horn" viewing deep space and a "calibration load" at instrument ambient temperature, at the scan extremes.

The Seasat SMMR data processing is shown schematically in Fig. 24. The SMMR digital bit stream is extracted from the satellite data stream in the early stages of ground processing to form the Sensor Data Record (SDR). This contains the SMMR radiometric, engineering, and housekeeping data, in addition to satellite and footprint location data. The SDR is input to the calibration processing, which converts the digital radiom-

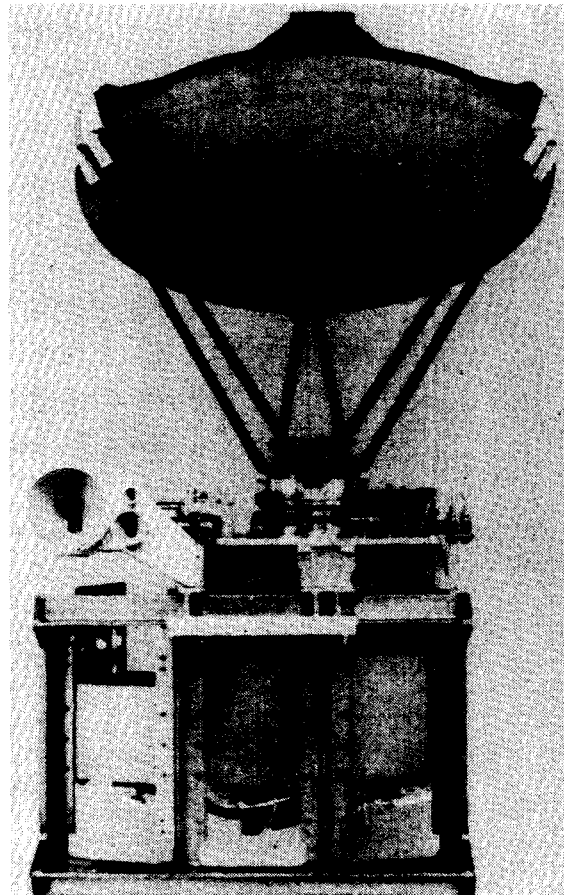


Fig. 22. Photograph showing front view of SMMR instrument (*Seasat* and *Nimbus-7*).

eter output data into antenna temperatures [63]. The antenna temperatures are input to the antenna pattern correction algorithms, which reformat the data, compensate for antenna side-lobe and cross-polarization effects, and perform a number of other supplementary operations such as corrections for spacecraft attitude and data quality flagging [64]. The brightness temperature data are then passed on to the final stage of data processing in which the geophysical parameters are derived.

The ocean-parameter retrieval algorithms are based on physical models of the effects of surface temperature and wind speed on brightness temperature [18]. The 6.6-GHz frequency was chosen for sensitivity to sea-surface temperature (SST). At 10.69 GHz, there is increased sensitivity to wind speed but little contamination by atmospheric effects. The 18-, 21-, and 37-GHz frequencies collectively provide information on atmospheric water vapor, cloud liquid water, and rainfall, and make corrections for these effects at the lower frequencies (see Fig. 2). Dual polarization is used at all frequencies to provide additional discriminatory capability. In practice, combinations of particular brightness temperatures are used in the derivation of each parameter, as determined by regression analyses or other retrieval techniques. The dual-polarization multifrequency capability is also used for improved discrimination of ice types and measurement of snow properties.

Initial results of comparisons between Seasat SMMR measurements and data from other sources have been described by Lipes *et al.* [65], [72] and Hofer *et al.* [66]. Fig. 25 shows the results of point comparisons between Seasat SMMR and conventional SST measurements in the Pacific Ocean. The

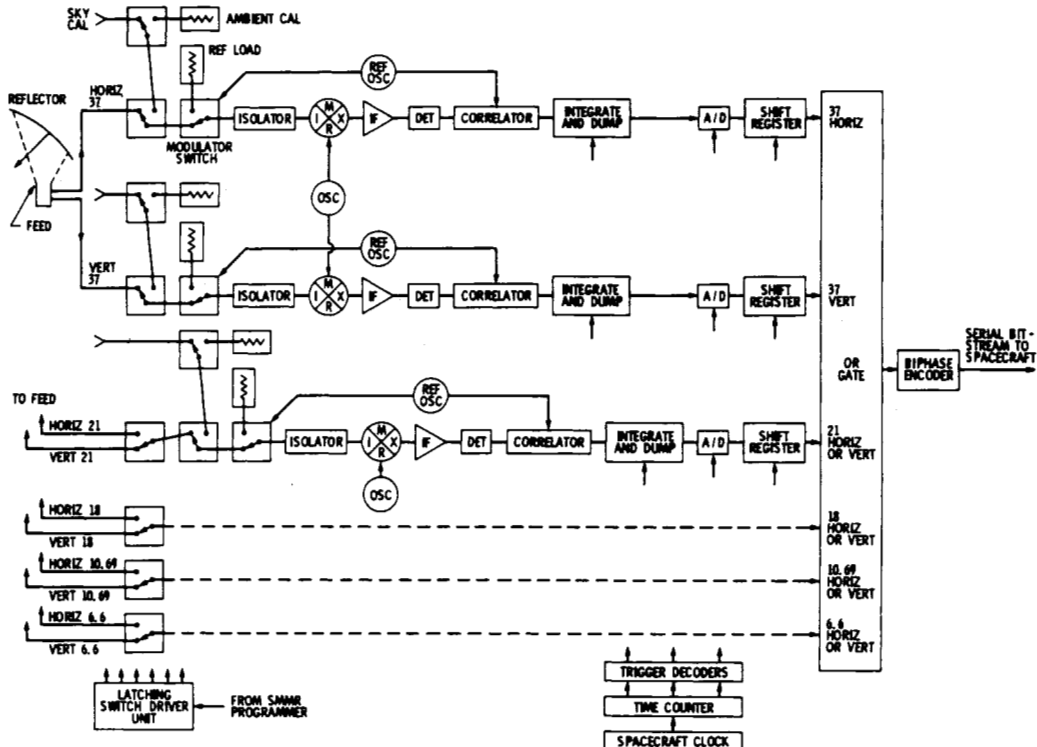
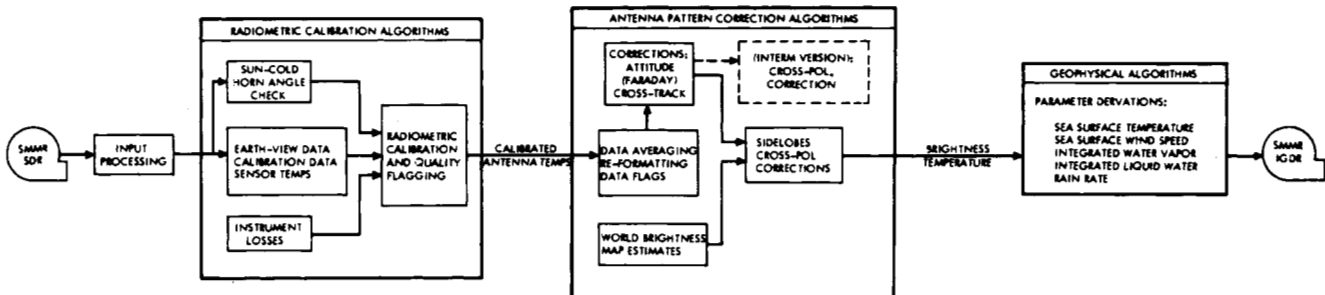
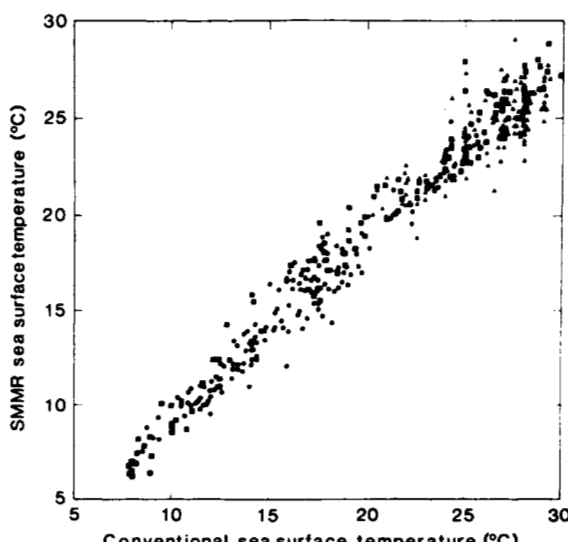


Fig. 23. SMMR instrument functional block diagram.

Fig. 24. Seasat SMMR data processing flow diagram (after Njoku *et al.* [30]).Fig. 25. Comparisons of Seasat SMMR retrieved sea surface temperature measurements and conventional XBT and ship measurements in the Pacific Ocean (after Hofer *et al.* [66]).

rms discrepancy between the two data sets is approximately 1.2 K. A 12-day-average SMMR global SST map for July, 1978 is shown in Fig. 26. Contours near coastal regions and inland waters may be unreliable, but in open ocean areas ( $\sim 600$  km from land) the map is believed accurate to about 1 K. A scatter plot of SMMR wind-speed measurements versus winds derived from surface observations in the N.E. Pacific is shown in Fig. 27. The rms discrepancy is approximately 2 m/s which is close to the expected accuracy of the surface measurements themselves. Continuing analysis of SMMR data from both Seasat and Nimbus-7 satellites will enable studies of a global nature to be performed for oceanography, weather, and climate applications.

#### H. Other Sensors

In addition to progress made in the U.S. represented by the evolution of sensors described above, other nations, notably the U.S.S.R., Europe, Japan, and India have also developed plans for the utilization of microwave radiometry from space. As shown in Table I, the radiometers aboard the Soviet Cosmos-243 and -384 satellites provided the first microwave views of



Fig. 26. Global sea surface temperature contour map derived from Seasat SMMR data, July 13-24, 1978.

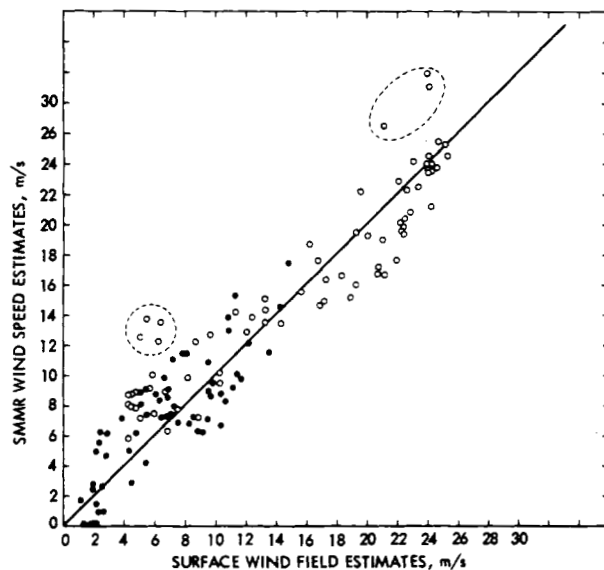


Fig. 27 SMMR retrieved wind comparisons with surface truth winds derived by kinematic analysis. Comparisons are for two satellite passes over the Gulf of Alaska region. (Circled points correspond to unreliable surface truth.) (After Lipes [72].)

the earth from space. The two lower frequencies on Cosmos-243, 3.5 and 8.8 GHz, provided information on surface conditions, while the two higher frequencies, 22.2 and 37 GHz, were used to estimate atmospheric water vapor and liquid water [6]. Results from Cosmos-243 are shown in Fig. 28. Fig. 28(a) shows estimates of surface temperature in the Pacific Ocean as compared with mean climatic data and with ship reports at the higher latitudes. Fig. 28(b) shows brightness temperature variations over the Antarctic, and indicates the contrast observed at frequencies of 8.8 and 22.2 GHz between the open ocean, floating sea ice, and various regions of continental ice. The Cosmos-384 satellite, launched two years after Cosmos-243 in 1970, carried the same frequencies and had similar objectives [67]. The U.S.S.R. launched its Intercosmos-20

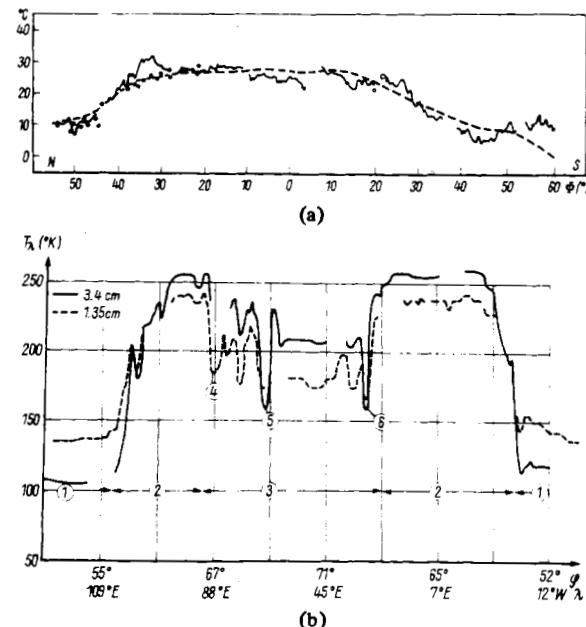


Fig. 28. Results from Cosmos-243 radiometers. (a) Surface temperature estimates in the Pacific Ocean compared with climatology (dashed line) and ship reports (circles). (b) Brightness temperature variations over the Antarctic continent, showing ① open sea, ② sea ice, ③ continental ice (including ④, ⑤, and ⑥: Western, Amery, and Lasarev barrier glaciers, respectively). (After Basharinov *et al.* [6].)

satellite in 1980, which had a microwave radiometer on board for making oceanographic measurements including surface temperature and wind speed [68].

India launched its first remote-sensing satellite "Bhaskara" in June 1979, which included a Satellite Microwave Radiometer (SAMIR) operating at frequencies of 19.1 and 22 GHz. Objectives of SAMIR were primarily to monitor atmospheric water vapor and liquid water in relation to studies of the Indian Monsoon. The instrument and initial results have been described by Pandey *et al.* [69]. A second, similar instrument was launched in November, 1981.

## V. FUTURE DEVELOPMENTS

During the past decade, passive microwave remote sensing from space has made dramatic progress. For several applications, spaceborne microwave sensors have demonstrated their potential for becoming beneficial components of global monitoring systems. This potential will quite possibly be realized during the 1980's, and new applications will be advanced, as technology and data utilization capabilities continue to develop. As the applications proliferate and new sensor types evolve, it is clear that some coordination is required to design efficient sensors that can satisfy broad groups of satellite data users in a way that is economic and yet satisfies the various foreseeable government and commercial program objectives. In an attempt to provide insight into some of these issues a panel comprising instrument scientists, researchers, and operational data users was assembled by NASA in 1977 to review the current state of the art, and to make recommendations on directions which future system developments should take. This Applications Review Panel (ARP) produced a final report [70] whose contents are highly relevant to the discussion in this section and which will be referred to as appropriate.

### A. Applications

Applications of passive microwave systems in space may be divided into two broad groups, those that require imaging of the earth and atmosphere beneath the satellite, and those that require viewing of the earth's atmosphere at the planetary limb. The primary earth-imaging applications are listed in Table III (adapted from the ARP report). The spatial resolutions, receiver sensitivities, and revisit times needed to satisfy these applications with respect to the various parameters of interest are also listed. In order to assess the ability of a single system to jointly satisfy several of these application requirements, the ARP report selected a baseline system for discussion based on technology available in the early 1980's. The baseline system had a 4-m mechanically scanned antenna compatible with a Shuttle launch. The spatial resolution and sensitivity achievable with this system for each of the listed applications are also given in Table III for a satellite altitude of 900 km. The table is discussed further in Section V-B.

For synoptic meteorology and climatology applications, passive microwave sensors are beginning to be exploited operationally to supplement the traditional passive sensors in the infrared and visible regions of the spectrum. Examples are the microwave temperature sounders: MSU on TIROS-N, and SSM on DMSP Block 5. In addition to atmospheric temperature measurements or pressure-level thickness determinations, the oxygen-channel brightness temperature gradients are also useful in deriving wind fields at different levels in the atmosphere, particularly for geostrophic winds. To date, the temperature sounding instruments have had horizontal resolutions in excess of 100 km, making them useful only for observing synoptic-scale meteorological systems. Such sensors would be of even greater value if instruments having smaller fields of view were available to probe cloud-shielded subsynoptic and mesoscale weather situations. Within the tropical environment, knowledge of the large variations in water vapor are of great importance in understanding the development of tropical cyclones and cloud clusters. Most numerical prediction models require at least two vertical layers of water vapor amounts in the atmosphere rather than the total (integrated) amounts derived from previous microwave instruments. Utilization of the 183-GHz water vapor line in addition to the line at 22.2 GHz may improve the ability to derive water

vapor profile information. For operational use in these applications, satellite data with complete global coverage approximately every 6 h are desirable.

In severe storm applications the time scales of interest are short ( $\sim 1$  h) and the spatial scales are small ( $\sim 10$  km); thus the use of geostationary platforms and higher frequencies such as the 118-GHz O<sub>2</sub> line and the 183-GHz H<sub>2</sub>O line become desirable. Key measurement parameters, in addition to atmospheric temperature profile and water vapor, are precipitation and sea-surface winds. Precipitation has been observed over the oceans using ESMR data at 19.35 and 37 GHz, although the measurements suffer from modeling difficulties and coarse spatial resolution with respect to dimensions of typical rain cells. The use of frequencies above the 60-GHz oxygen complex shows promise for more quantitative rain measurements over both ocean and land areas. Studies of hurricanes and tropical cyclones using microwave data from Nimbus-5 and -6 sensors have shown much potential in storm forecasting studies and in understanding storm development. These applications will be much improved by sensors with better time and spatial resolution.

Ocean remote-sensing applications using microwave radiometers are in an early stage of development. The primary measurement requirements are for surface temperature, surface winds, and salinity. Oil slick detection and pollution monitoring are further possibilities [71]. The applications can be broadly classified into two groups. Open-ocean phenomena typically have large-scale features on the order of tens of kilometers with variabilities on time scales of a few days. These can be studied using wide-area observational coverage by spacecraft sensors at medium spatial resolutions (10–50 km). The results can be applied to medium- to long-range weather forecasting, and large-scale modeling of ocean dynamics and air-sea interactions. Coastal applications, on the other hand, focus on localized currents and smaller scale eddies which generally require spatial resolutions of less than 5 km, and on salinity and pollution monitoring, typically requiring resolutions of less than 1 km. The low microwave frequencies (1 to 10 GHz) necessary for making the ocean-surface measurements combined with the need for high spatial resolution in some of the applications is a driving force towards the development of larger space antennas. The SMMR instruments on Seasat and Nimbus-7 have provided the first steps in ocean microwave sensing from orbit, and more advanced sensors are in the planning stages.

Sea and land ice applications have received a promising start from measurements made by NEMS, SCAMS, and the ESMR's on Nimbus-5 and -6, and more recently by the SMMR on Nimbus-7 and Seasat. The principal measurement goals are the determination of temporal and spatial variations of sea-ice concentration and type, and horizontal and vertical temperature distributions and snow-accumulation rates on the ice sheets of Greenland and Antarctica. These measurements are important in advancing the understanding of ice dynamics, improving maritime operations and ship navigation in polar regions, and in climate modeling studies. For these applications, improved spatial resolutions of less than 5 km would aid in the location of specific large leads in the ice pack and enable more accurate ice-concentration determinations to be made.

Passive microwave sensing of land parameters, such as soil moisture and snowpack water equivalent, is far from maturity. This is mainly due to the variable nature of terrain surfaces and the poor spatial resolutions of current space sensors for

**TABLE III**  
**APPLICATIONS AND OBSERVABLE PARAMETERS FOR HIGH-RESOLUTION**  
**PASSIVE MICROWAVE SATELLITES**  
**(Adapted from [70].)**

APPLICATION AREAS AND OBSERVABLE PARAMETERS	DESIRED SPECIFICATIONS				[ $\Delta t_{\text{rms}}$ AT DESIRED RESOLUTION]	[ $\Delta t_{\text{rms}}$ AT CRITICAL FREQUENCY]	SPOT SIZE (KM)	HEIGHT (KM)	HEIGHT (KM)	HEIGHT (KM)	[ $\Delta t_{\text{rms}}$ AT DESIRED RESOLUTION]	[ $\Delta t_{\text{rms}}$ (AVAILABLE) vs ( $\Delta t_{\text{rms}}$ REQUIRED)]	FREQUENCY (GHz) SMR						TIROS-N			
	SPOT SIZE (KM)	$\Delta t_{\text{rms}}$	REVISIT TIME (HR)	HEIGHT (KM)				900	900	900	900		1.4	3.0	6.6	10.7	18	21	37	55	90	183
<b>SYNTHETIC METEOROLOGY &amp; CLIMATOLOGY</b>																						
Temperature Profile	50	0.3	3-12	3.3	0.3	0.06	1.1							-	⊕							
Water Vapor Profile	15	0.5	3-12	8.6	0.6	0.6	1.2							+	⊕	+						+
Water Vapor Profile (Non-Tropical)	15	0.5	3-12	1.0	3.0	0.06	6.0							-	+	+	+					+
Liquid Water Abundance, Rain Rate	2-10	2	3-12	4.9	1.3	0.5	0.6							-	⊕	+	-					+
Sea Surface Temperature	50	0.3	6-36	28	0.1	0.6	0.4							-	+	+	+					+
Sea Surface Wind (Magnitude)	50	1	3-12	1.7	0.1	0.3	0.1							-	⊕	+	+					+
Sea Surface Wind (No Precipitation)	50	1	3-12	4.9	0.2	0.1	0.2							-	⊕	+	+					+
<b>SEVERE STORMS</b>																						
Temperature Profile	3-30	0.3	1-6	3.3	0.6	0.11	1.9							-	⊕	+						+
Water Vapor Profile	3-15	0.5	1-6	8.6	0.6	0.4	1.2							-	⊕	+	+					+
Water Vapor Profile (Non-Tropical)	3-15	0.5	1-6	1.0	3.0	0.06	6.0							-	⊕	+	+					+
Liquid Water Abundance, Rain Rate	2-10	2	1-6	4.9	1.3	0.5	0.6							-	⊕	+	-					+
Sea Surface Temperature	3-30	0.3	2-6	28	0.2	0.9	0.6							-	⊕	+	+					+
Sea Surface Wind (Magnitude)	3-30	1	1-6	16.9	0.2	0.6	0.2							-	⊕	+	+					+
Sea Surface Wind (No Precipitation)	3-30	1	1-6	4.9	0.4	0.2	0.4							-	⊕	+	+					+
<b>OCEAN SURFACE</b>																						
Surface Wind Velocity	2-50	1	3-12	16.9	0.1	0.3	0.1							-	⊕	+	+					+
Surface Wind Velocity (No Precipitation)	10-15	1	3-12	4.9	0.2	0.1	0.2							-	⊕	+	+					+
Sea Surface Temperature	1-50	0.3	6-36	28	0.1	0.6	0.4							-	⊕	+	+					+
Salinity	0.5-10	0.3	3-12	1.30	0.5	13.0	1.6							-	⊕	+	+					+
Oil Slicks, etc. (No Precipitation)	0.5	0.3	1-12	4.9	25	9.8	84							-	⊕	+	+					+
<b>LAND PARAMETERS</b>																						
Soil Moisture (Low Frequency)	3-25	1	6-36	130	0.2	5.2	0.2							-	⊕	+	+					+
Soil Moisture (Higher Frequency)	3-25	1	6-36	28	0.2	1.1	0.2							-	⊕	+	+					+
Snow Cover and Type, Frozen Ground	3-25	1	6-12	4.9	0.5	0.2	0.5							-	⊕	+	+					+
<b>SEA AND LAND ICE</b>																						
Sea Ice Concentration	1-5	2	3-12	4.9	2.5	1.0	1.3							-	⊕	+	+					+
Sea Ice Type	1-5	1	6-12	4.9	2.5	1.0	2.5							-	⊕	+	+					+
Land Ice Properties (e.g., Firm)	10-50	1	12-36	4.9	0.2	0.1	0.2							-	⊕	+	+					+

making these measurements. In water resources applications, soil-moisture information can be applied in hydrological models for predicting runoff and flood conditions. Similarly, snowpack measurements can be used to estimate spring runoff and melt water. Both applications require data with resolution on the order of less than 3 km. For agricultural applications, where soil-moisture information is used in crop yield forecasting models and large-area resource planning, spatial resolutions of about 10 km are desirable. For studies of the effects of soil moisture and snow cover on climate, somewhat larger spatial resolution is acceptable. Soil moisture is best measured using low frequencies in the 1- to 3-GHz range, where depth penetration on the order of centimeters can be achieved, and confusing effects of surface vegetation and roughness are minimized. For snowpack monitoring, a multifrequency approach is most promising, using several frequencies in the range 3 to 90 GHz.

Microwave sensing of the earth's upper atmosphere (stratosphere, mesosphere, and lower thermosphere) is a relatively new application. Global measurements in the upper atmosphere of the abundances of several molecular species, and measurements of temperature, winds, magnetic field, and reference pressure levels, will assist in understanding the complex chemistry and transport processes of that region. Limb-sounding techniques are best suited to these measurements since they provide substantially improved sensitivities and vertical resolutions over downward-looking experiments. With such techniques, several important measurements can be made using existing technology. The extension of microwave technology to submillimeter wavelengths will allow many more important measurements to be made.

#### B. Technology Advancement

The improvement in characteristics of the various spacecraft sensors described in previous sections, and the expanding applications and requirements discussed above, lead naturally to a discussion of the technological capabilities for meeting these requirements in the 1980's. In addition, as pointed out in the ARP report [70], there are substantial economic benefits to be gained in satisfying a large number of applications by using a few versatile system designs. This is especially true of applications that require improved spatial resolutions and hence larger and more costly antennas. A suggested possibility for the near term is the use of a 4-m offset-fed parabolic reflector antenna which could be stowed for launch within the Shuttle payload bay, and when deployed in space could be scanned mechanically at a rate of up to about 60 r/min. This type of antenna was used as a baseline for deriving the performance characteristics presented in Table III. An off-axis feed location was chosen to avoid blockage and to provide high beam efficiency. The antenna would scan about a vertical axis causing the beam to sweep out a conical surface, with a constant incidence angle at its intersection with the earth. For the purpose of the calculations in Table III an incidence angle of 55° was assumed, the sum of the receiver noise temperature and the antenna temperature was assumed to be  $(400 + 20\nu)$  K, where  $\nu$  is the radiometer frequency in gigahertz, and the receiver bandwidth for each channel was assumed to be 100 MHz. These numbers may vary in actual systems but are good baseline approximations. The table also suggests a range of frequencies which could be used to serve the listed applications. These frequencies are indicated by three symbols: + indicates frequencies that are of primary importance, · indicates helpful secondary frequencies, and ⊕ indicates the "critical" frequency

for which the spatial resolution was determined for the purposes of the analysis.

By studying Table III it can be seen that the critical frequency spot size is significantly greater than the maximum desired spot size only for the salinity, oil slick, and soil-moisture measurements. To meet the requirements of these applications, much larger antenna systems are required. A number of other parameters appear to have marginal resolutions, but useful information could nevertheless be obtained. High spatial resolution implies short integration times, and certain applications may, therefore, require receiver sensitivities that are unobtainable. With a foreseeable future doubling of receiver sensitivities, only the water vapor determinations using 183 GHz appear to have serious problems for lack of sensitivity. Cryogenic receivers could solve this problem.

The ARP study report suggested four classifications of systems for future passive microwave sensing from orbit: 1) A system of the kind described above, providing full earth coverage and satisfying the majority of applications; 2) large, specialized antenna systems designed for low-frequency high-resolution applications such as salinity and soil moisture; 3) geosynchronous atmospheric sounders operating around the O<sub>2</sub> and H<sub>2</sub>O resonance frequencies; 4) limb-scanning systems for upper atmospheric studies. Development of such systems will depend largely on the priorities assigned to the various applications.

#### VI. DISCUSSION

This paper has reviewed the development of passive microwave remote sensors as applied to earth observations from space. In the temperature sounding application the technique has reached the operational stage with the implementation of the MSU. An advanced version of this instrument with extended capabilities, the AMSU, is currently being planned by NOAA and NASA. A limited-operational sensor for oceanographic applications has also been discussed by the U.S. Navy, NOAA, and NASA, to meet the growing needs for continuous global oceanographic data sets. However, an increasingly careful scrutiny is being placed on new developments in these areas due to the high operational costs. It is hoped that continuing emphasis can be maintained on the experimental and operational demonstrations in order that the momentum gained during the past decade of microwave radiometry from space is not lost.

#### REFERENCES

- [1] D. H. Staelin, "Passive remote sensing at microwave wavelengths," *Proc. IEEE*, vol. 57, no. 4, 1969.
- [2] —, "Passive microwave techniques for geophysical sensing of the earth from satellites," *IEEE Trans. Antennas Propagat.*, vol. AP-29, pp. 683-687, July 1981.
- [3] K. Tomiyasu, "Remote sensing of the earth by microwaves," *Proc. IEEE*, vol. 62, no. 1, 1974.
- [4] R. H. Dicke, R. Beringer, R. L. Kyhl, and A. B. Vane, "Atmospheric absorption measurements with a microwave radiometer," *Phys. Rev.*, vol. 70, p. 340, 1946.
- [5] F. T. Barath, A. H. Barrett, J. Copeland, D. E. Jones, and A. E. Lilley, "Mariner 2 microwave radiometer experiment and results," *Astron. J.*, vol. 69, no. 1, 1964.
- [6] A. E. Basharinov, A. S. Gurvich, S. T. Yegorov, A. A. Kurskaya, D. T. Matveyev, and A. M. Shutko, "The results of microwave sounding of the earth's surface according to experimental data from the satellite Cosmos 243," in *Space Research XI*. Berlin: Akademie-Verlag, 1971.
- [7] J. W. Waters, "Absorption and emission by atmospheric gases," in *Methods of Experimental Physics*, vol. 12, p. B, M. L. Meeks, Ed. New York: Academic Press, 1976, pp. 172-176.
- [8] M. L. Meeks and A. E. Lilley, "The microwave spectrum of oxygen in the earth's atmosphere," *J. Geophys. Res.*, vol. 68, p. 1683, 1963.

- [9] W. B. Lenoir, "Microwave spectrum of molecular oxygen in the mesosphere," *J. Geophys. Res.*, vol. 73, p. 361, 1968.
- [10] J. W. Waters and D. H. Staelin, "Statistical inversion of radiometric data," *Quart. Progr. Rep.* 89, MIT Research Lab. of Electronics, Cambridge, MA, 1968.
- [11] J. W. Waters, K. F. Kunzi, R. L. Pettyjohn, R. K. L. Poon, and D. H. Staelin, "Remote sensing of atmospheric temperature profiles with the Nimbus-5 microwave spectrometer," *J. Atm. Sci.*, vol. 32, no. 10, 1975.
- [12] D. H. Staelin, A. L. Cassel, K. F. Kunzi, R. L. Pettyjohn, R. K. L. Poon, P. W. Rosenkranz, and J. W. Waters, "Microwave atmospheric temperature sounding: effects of clouds on the Nimbus-5 satellite data," *J. Atm. Sci.*, vol. 32, p. 1970, 1975.
- [13] D. H. Staelin, K. F. Kunzi, R. L. Pettyjohn, R. K. L. Poon, R. W. Wilcox, and J. W. Waters, "Remote sensing of atmospheric water vapor and liquid water with the Nimbus-5 microwave spectrometer," *J. Appl. Meteorol.*, vol. 15, no. 11, 1976.
- [14] N. C. Grody and P. P. Pellegrino, "Synoptic-scale studies using Nimbus-G scanning microwave spectrometer," *J. Appl. Meteorol.*, vol. 16, p. 816, 1977.
- [15] P. W. Rosenkranz, D. H. Staelin, and N. C. Grody, "Typhoon June (1975) viewed by a scanning microwave spectrometer," *J. Geophys. Res.*, vol. 83, no. C4, 1978.
- [16] T. T. Wilheit, R. R. Adler, R. Burpee, R. Sheets, W. E. Shenk, and P. W. Rosenkranz, "Monitoring of severe storms," in *High Resolution Passive Microwave Satellites*, D. H. Staelin and P. W. Rosenkranz, Eds., MIT Research Lab. of Electronics, Cambridge, MA, 1978.
- [17] J. W. Waters and S. C. Wofsy, "Applications of high resolution passive microwave satellite systems to the stratosphere, mesosphere, and lower thermosphere," in *High Resolution Passive Microwave Satellites*, D. H. Staelin and P. W. Rosenkranz, Eds., MIT Research Lab. of Electronics, Cambridge, MA, 1978.
- [18] T. T. Wilheit, "A review of applications of microwave radiometry to oceanography," *Boundary-Layer Meteorol.*, vol. 13, pp. 277-293, 1978.
- [19] T. Wilheit, A. T. C. Chang, and A. S. Milman, "Atmospheric corrections to passive microwave observations of the ocean," *Boundary-Layer Meteorol.*, vol. 18, pp. 65-77, 1980.
- [20] C. T. Swift, "Passive microwave remote sensing of the ocean—A review," *Boundary-Layer Meteorol.*, vol. 18, pp. 25-54, 1980.
- [21] P. Gloersen, H. J. Zwally, A. T. C. Chang, D. K. Hall, W. J. Campbell, and R. D. Ramseier, "Time-dependence of sea-ice concentration and multiyear ice fraction in the arctic basin," *Boundary-Layer Meteorol.*, vol. 13, pp. 339-359, 1978.
- [22] T. J. Schmugge, "Microwave approaches in hydrology," *Photogramm. Eng. Remote Sensing*, vol. 46, pp. 495-507, Apr. 1980.
- [23] K. F. Kunzi, A. D. Fisher, D. H. Staelin, and J. W. Waters, "Snow and ice surfaces measured by the Nimbus-5 microwave spectrometer," *J. Geophys. Res.*, vol. 81, no. 27, 1976.
- [24] H. J. Zwally and P. Gloersen, "Passive microwave images of the polar regions and research applications," *Polar Rec.*, vol. 18, no. 116, 1976.
- [25] T. T. Wilheit, J. S. Theon, W. E. Shenk, L. J. Allison, and E. B. Rodgers, "Meteorological interpretations of the images from the Nimbus-5 electrically scanned microwave radiometer," *J. Appl. Meteorol.*, vol. 15, p. 166, 1976.
- [26] T. T. Wilheit, A. T. C. Chang, M. S. V. Rao, E. B. Rodgers, and J. S. Theon, "A satellite technique for quantitatively mapping rainfall rates over the oceans," *J. Appl. Meteorol.*, vol. 16, p. 551, 1977.
- [27] A. Sobti and R. K. Moore, "Correlation between microwave scattering and emission from land and sea," *IEEE Trans. Geosci. Electron.*, vol. GE-14, no. 2, 1976.
- [28] J. R. Eagleton and W. C. Lin, "Remote sensing of soil moisture by a 21-cm passive radiometer," *J. Geophys. Res.*, vol. 81, no. 21, 1976.
- [29] P. Gloersen and F. T. Barath, "A scanning multi-channel microwave radiometer for Nimbus-G and Seasat-A," *IEEE J. Oceanic Eng.*, vol. OE-2, no. 2, 1977.
- [30] E. G. Njoku, J. M. Stacey, and F. T. Barath, "The Seasat scanning multichannel microwave radiometer (SMMR): Instrument description and performance," *IEEE J. Oceanic Eng.*, vol. OE-5, no. 2, 1980.
- [31] L. A. Klein and C. T. Swift, "An improved model for the dielectric constant of sea water at microwave frequencies," *IEEE Trans. Antennas Propagat.*, vol. AP-25, p. 104, 1977.
- [32] H. C. Blume, B. M. Kendall, and J. C. Fedors, "Measurements of ocean temperature and salinity via microwave radiometry," *Boundary-Layer Meteorol.*, vol. 13, p. 295, 1978.
- [33] W. Nordberg, J. Conaway, D. B. Ross, and T. Wilheit, "Measurements of microwave emission from a foam-covered, wind-driven sea," *J. Atm. Sci.*, vol. 28, p. 429, 1971.
- [34] J. P. Hollinger, "Passive microwave measurements of sea surface roughness," *IEEE Trans. Geosci. Electron.*, vol. GE-9, p. 165, 1971.
- [35] W. J. Webster, T. T. Wilheit, D. B. Ross, and P. Gloersen, "Spec-tral characteristics of the microwave emission from a wind-driven, foam-covered sea," *J. Geophys. Res.*, vol. 81, p. 3095, 1976.
- [36] T. T. Wilheit, "A model for the microwave emissivity of the ocean's surface as a function of wind speed," *IEEE Trans. Geosci. Electron.*, vol. GE-17, pp. 244-249, 1979.
- [37] J. D. Kraus, *Radio Astronomy*. New York: McGraw-Hill, 1966.
- [38] Hughes Aircraft Co., "Special sensor microwave/imager (SSM/I), overall preliminary design review," Hughes Aircraft Co., El Segundo, CA, Nov. 1979.
- [39] R. M. Price, "Radiometer fundamentals," in *Methods of Experimental Physics*, vol. 12, pt B, M. L. Meeks, Ed. New York: Academic Press, 1976, pp. 210-222.
- [40] J. C. King, "Quantization and symmetry in periodic coverage patterns with applications to earth observation," *J. Astro. Sci.*, vol. XXIV, no. 4, 1976.
- [41] D. H. Staelin, F. T. Barath, J. C. Blinn, and E. J. Johnston, "The Nimbus-E microwave spectrometer (NEMS) experiment," in *The Nimbus-5 User's Guide*. Greenbelt, MD: NASA/Goddard Space Flight Center, 1972.
- [42] N. C. Grody, "Remote sensing of atmospheric water content from satellites using microwave radiometry," *IEEE Trans. Antennas Propagat.*, vol. AP-24, no. 2, 1976.
- [43] T. T. Wilheit, "The electrically scanning microwave radiometer (ESMR) experiment," in *The Nimbus-5 User's Guide*. Greenbelt, MD: NASA/Goddard Space Flight Center, 1972.
- [44] P. Gloersen, T. T. Wilheit, T. C. Chang, W. Nordberg, and W. J. Campbell, "Microwave maps of the polar ice of the earth," *Bull. Amer. Met. Soc.*, vol. 55, no. 12, 1974.
- [45] P. Gloersen and V. V. Salomonson, "Satellites—New global observing techniques for ice and snow," *J. Glaciology*, vol. 15, no. 73, 1975.
- [46] W. J. Campbell, P. Gloersen, W. J. Webster, T. T. Wilheit, and R. O. Ramseier, "Beaufort sea ice zones as delineated by microwave imagery," *J. Geophys. Res.*, vol. 81, no. 6, 1976.
- [47] P. Gloersen, H. J. Zwally, A. T. C. Chang, D. K. Hall, W. J. Campbell, and R. O. Ramseier, "Time-dependence of sea-ice concentration and multiyear ice fraction in the Arctic basin," *Boundary-Layer Meteorol.*, vol. 13, p. 339, 1978.
- [48] L. J. Allison, E. B. Rodgers, T. T. Wilheit, and R. W. Fett, "Tropical cyclone rainfall as measured by the Nimbus-5 electrically scanning microwave radiometer," *Bull. Amer. Met. Soc.*, vol. 55, no. 9, 1974.
- [49] R. F. Adler and E. B. Rodgers, "Satellite-observed latent heat release in a tropical cyclone," *Mon. Weather Rev.*, vol. 105, p. 956, 1977.
- [50] T. J. Schmugge, J. M. Meneely, A. Rango, and R. Neff, "Satellite microwave observations of soil moisture variations," *Water Resources Bull.*, vol. 13, no. 2, 1977.
- [51] A. E. Potter, C. K. Williams, A. L. Grandfield, K. J. Demel, M. C. Trichel, T. L. Barnett, R. D. Judy, W. E. Hensley, N. M. Hatcher, W. E. McAllum, J. T. McGoogan, J. C. Jones, O. N. Brandt, J. G. Braithwaite, R. H. McLaughlin, R. Collins, W. H. Peake, and R. K. Moore, "Summary of flight performance of the Skylab earth resources experimental package (EREP)," in *Proc. 9th Int. Symp. on Remote Sensing of the Environment* (Ann Arbor, MI), p. 1803, 1974.
- [52] R. K. Moore, J. P. Claassen, A. C. Cook, D. L. Fayman, J. C. Holtzman, A. Sobti, W. E. Spencer, F. T. Ulaby, J. D. Young, W. J. Pierson, V. J. Cardone, J. Hayes, W. Spring, R. J. Kern, and N. M. Hatcher, "Simultaneous active and passive microwave responses of the earth—The Skylab Radscat experiment," in *Proc. 9th Int. Symp. on Remote Sensing of Environment* (Ann Arbor, MI), p. 189, 1974.
- [53] R. K. Moore, F. T. Ulaby, and A. Sobti, "The influence of soil moisture on the microwave response from terrain as seen from orbit," in *Proc. 10th Int. Symp. on Remote Sensing of Environment* (Ann Arbor, MI), 1975.
- [54] F. T. Ulaby, L. F. Dellwig, and T. Schmugge, "Satellite microwave observations of the Utah Great Salt Lake Desert," *Radio Sci.*, vol. 10, no. 11, 1975.
- [55] R. K. Moore and J. D. Young, "Active microwave measurements from space," *IEEE J. Oceanic Eng.*, vol. OE-2, no. 4, 1977.
- [56] M. J. McFarland, "The correlation of Skylab L-band brightness temperatures with antecedent precipitation," in *Proc. NASA Earth Resources Symp.*, NASA TMX-58168, p. 2243, 1976.
- [57] D. H. Staelin, A. H. Barrett, P. W. Rosenkranz, F. T. Barath, E. J. Johnston, J. W. Waters, A. Wouters, and W. B. Lenoir, "The scanning microwave spectrometer (SCAMS) experiment," in *The Nimbus-6 User's Guide*. Greenbelt, MD: NASA/Goddard Space Flight Center, 1975.
- [58] S. Q. Kidder, W. M. Gray, and T. H. Vonder Haar, "Estimating tropical cyclone central pressure and outer winds from satellite microwave data," *Mon. Weather Rev.*, vol. 106, p. 1458, 1978.
- [59] N. C. Grody, A. Gruber, and W. C. Shen, "Atmospheric water content over the tropical Pacific derived from the Nimbus-6 scanning microwave spectrometer," *J. Appl. Meteorol.*, vol. 19, p. 986, 1980.

- [60] T. T. Wilheit, "The electrically scanning microwave radiometer (ESMR) experiment," in *The Nimbus-6 User's Guide*. Greenbelt, MD: NASA/Goddard Space Flight Center, 1975.
- [61] T. T. Wilheit, "The effect of wind on the microwave emission from the ocean's surface at 37 GHz," *J. Geophys. Res.*, vol. 84, pp. 4921-4926, 1979.
- [62] J. A. Weinman and P. J. Guetter, "Determination of rainfall distributions from microwave radiation measured by the Nimbus-6 EMSR," *J. Appl. Met.*, vol. 16, pp. 437-442, 1977.
- [63] P. N. Swanson and A. L. Riley, "The Seasat scanning multichannel microwave radiometer (SMMR): Radiometric calibration algorithm development and performance," *IEEE J. Oceanic Eng.*, vol. OE-5 no. 2, 1980.
- [64] E. G. Njoku, E. J. Christensen, and R. E. Cofield, "The Seasat scanning multichannel microwave radiometer (SMMR): Antenna pattern corrections—development and implementation," *IEEE J. Oceanic Eng.*, vol. OE-5, no. 2, 1980.
- [65] R. G. Lipes, R. L. Bernstein, V. J. Cardone, K. G. Katsaros, E. G. Njoku, A. L. Riley, D. B. Ross, C. T. Swift, and F. J. Wentz, "Seasat scanning multichannel microwave radiometer: Results of the Gulf of Alaska workshop," *Science*, vol. 204, no. 4400, 1979.
- [66] R. Hofer, E. G. Njoku, and J. W. Waters, "Microwave radiometric measurements of sea surface temperature from the Seasat satellite: First results," *Science*, vol. 212, p. 1385, 1981.
- [67] A. E. Basharinov, A. S. Gurvitch, A. K. Gorodezky, S. T. Egorov, B. G. Kutuzova, A. A. Kurskaya, D. T. Matveev, A. P. Orlov, and A. M. Shutko, "Satellite measurements of microwave and infrared radiobrightness temperature of the earth's cover and clouds," in *Proc. 8th Int. Symp. on Remote Sensing of Environment* (Ann Arbor, MI), pp. 291-296, 1972.
- [68] A. M. Shutko, private communication, 1980.
- [69] P. C. Pandey, A. K. Sharma, and B. S. Gohil, "A simulation technique for the determination of atmospheric water content with Bhaskara satellite microwave radiometer (SAMIR)," *Proc. Indian Acad. Sci.*, vol. 90, pp. 105-110, 1981.
- [70] D. H. Staelin and P. W. Rosenkranz, Eds. *High Resolution Passive Microwave Satellites: Applications*. Review Panel Final Rep., MIT Research Lab. of Electronics, Cambridge, MA, 1978.
- [71] J. P. Hollinger and R. A. Mannella, "Oil spills: Measurement of their distributions and volumes by multifrequency microwave radiometry," *Science*, vol. 181, pp. 54-56, 1973.
- [72] R. G. Lipes, "SMMR Panel Report," in *Seasat-JASIN Workshop Rep.*, Publ. 80-62, vol. 1, pp. 5-51, Jet Propulsion Laboratory, Pasadena, CA, 1980.

## Time-Domain Skin-Effect Model for Transient Analysis of Lossy Transmission Lines

CHU-SUN YEN, MEMBER, IEEE, ZVONKO FAZARINC, AND RICHARD L. WHEELER, MEMBER, IEEE

**Abstract**—A skin-effect equivalent circuit consisting of resistors and inductors is derived from the skin-effect differential equations for simulating the loss of a transmission line. A numerical method is used to analyze the transmission-line differential equations and the skin-effect equivalent circuit, yielding a model which relates the new values of node voltages and line currents to their values at the previous time step. Based on this model, a very simple program was written on a desk-top computer for the transient analysis of lossy transmission lines.

Two examples are presented. The first example is an analysis of the step and pulse responses of a 600-m RG-8/U coaxial cable. The computed results show excellent agreement with measured data. The second example studies the current at the end of a 12-in 7- $\Omega$  strip line under different loading conditions. Very good agreement has been obtained between the calculated steady-state solution and that obtained by the frequency-domain method.

### I. INTRODUCTION

TRANSMISSION LINES with frequency-dependent skin-effect loss were analyzed by Wigington and Nahman in 1957 using the Laplace transform methods [1]. In this classical paper, the skin-effect loss is assumed to have the ideal square-root frequency dependency, and the lines are terminated by their characteristic impedances. The first-order approxima-

tion for the step response is given by the well-known complementary error function. Extension of this method to include practical frequency-dependent losses [2] or arbitrary resistive terminations [3] is not a trivial task. In 1964, computers were applied to the study of transmission lines by Bertin using the frequency-domain method. In this method, one first calculates the gain and phase change for each of the frequency components contained in the input waveform, and then reassembles them to obtain the time-domain response [4]. The frequency-domain method is not well suited for the time-domain transient analysis, since it provides only the steady-state response for repetitive input waveforms. This method also introduces frequency-windowing ripple to the output waveform.

A different approach is the method of characteristics for the time-domain analysis. It was first applied to lossless transmission lines by Branin in 1967 [5], and was later extended to transmission lines with constant, frequency-independent loss by Dommel in 1969 [6], and by Gruodis in 1979 [7]. The usefulness of these methods is limited to the low-frequency range where the frequency-dependent skin-effect loss can be neglected.

For transient analysis of transmission lines with skin-effect loss, one simple often used method is to include waveshaping at the end of a lossless transmission line [8]-[10]. The lossless transmission line is used to simulate the delay, and the

Manuscript received August 24, 1981; revised March 31, 1982 and June 1, 1982.

The authors are with Hewlett-Packard Laboratories, Palo Alto, CA 94304.

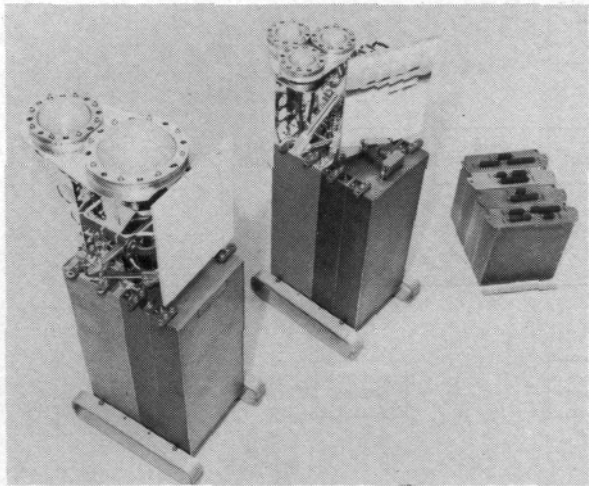


Fig. 6. Photograph of NEMS instrument (Nimbus-5) showing separate  $\text{H}_2\text{O}$  and  $\text{O}_2$  modules and power supply module.

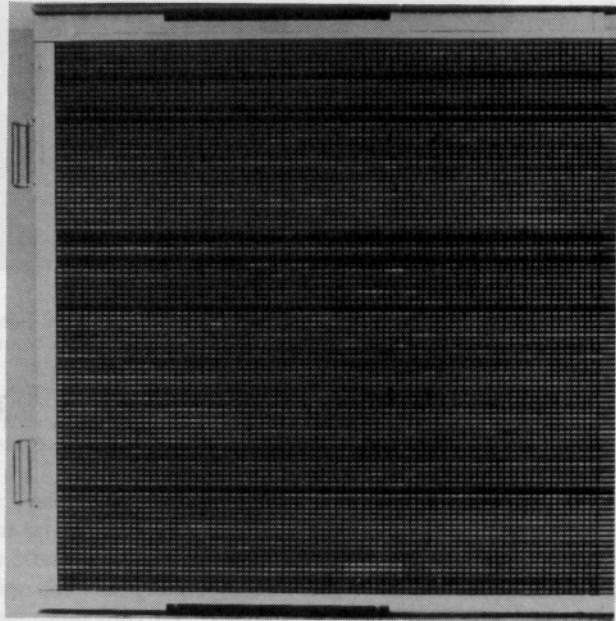


Fig. 13. Photograph of ESMR waveguide phased array antenna.

\*\* NORTH POLAR MICROWAVE BRIGHTNESS TEMPERATURE \*\*  
\* NIMBUS-5 ESMR (1.55 CM) 3-DAY AVERAGE \*  
\*\* JANUARY 15, 73 FROM 015 07 40 TO 017 22 51 \*\*

2282.5

280K

275K

270K

265K

260K

255K

250K

245K

240K

235K

230K

225K

220K

215K

210K

205K

200K

195K

190K

185K

180K

175K

170K

165K

160K

155K

150K

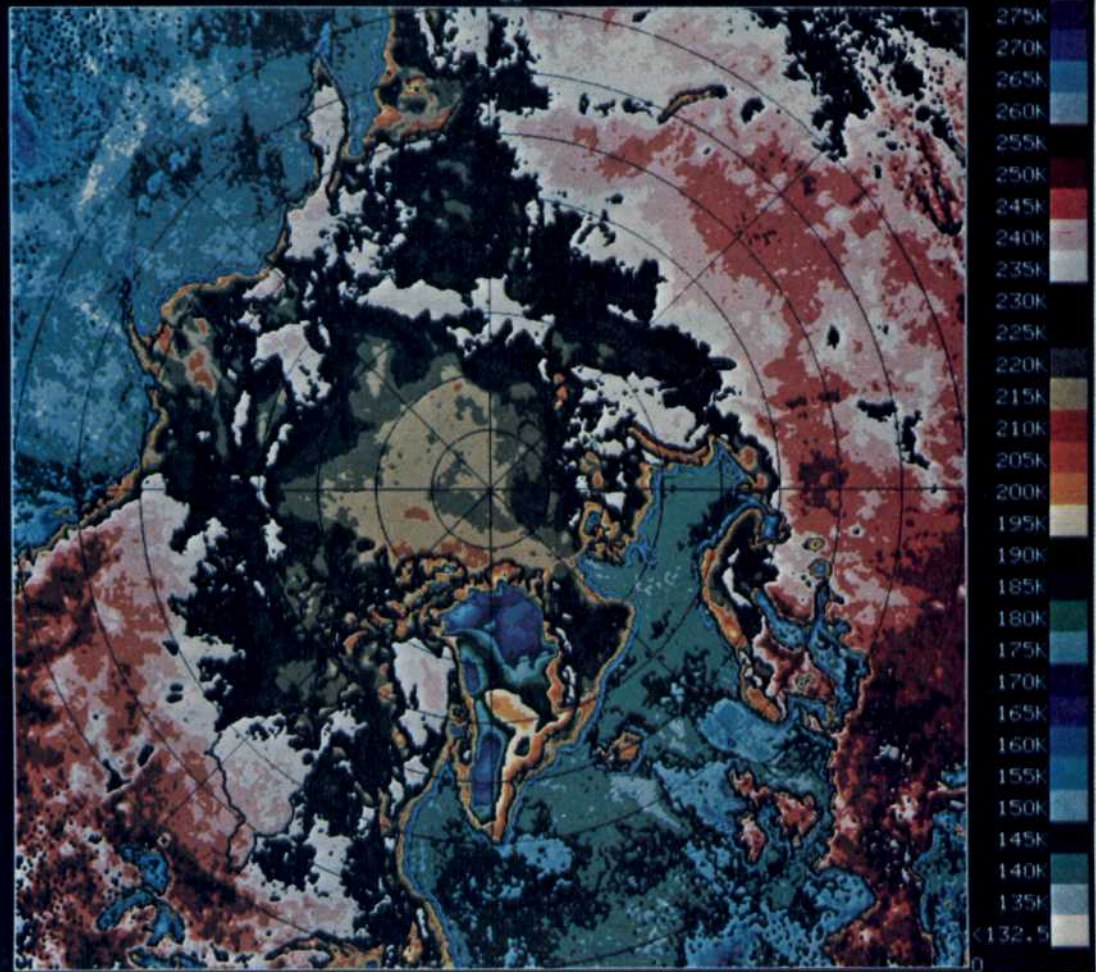
145K

140K

135K

132.5

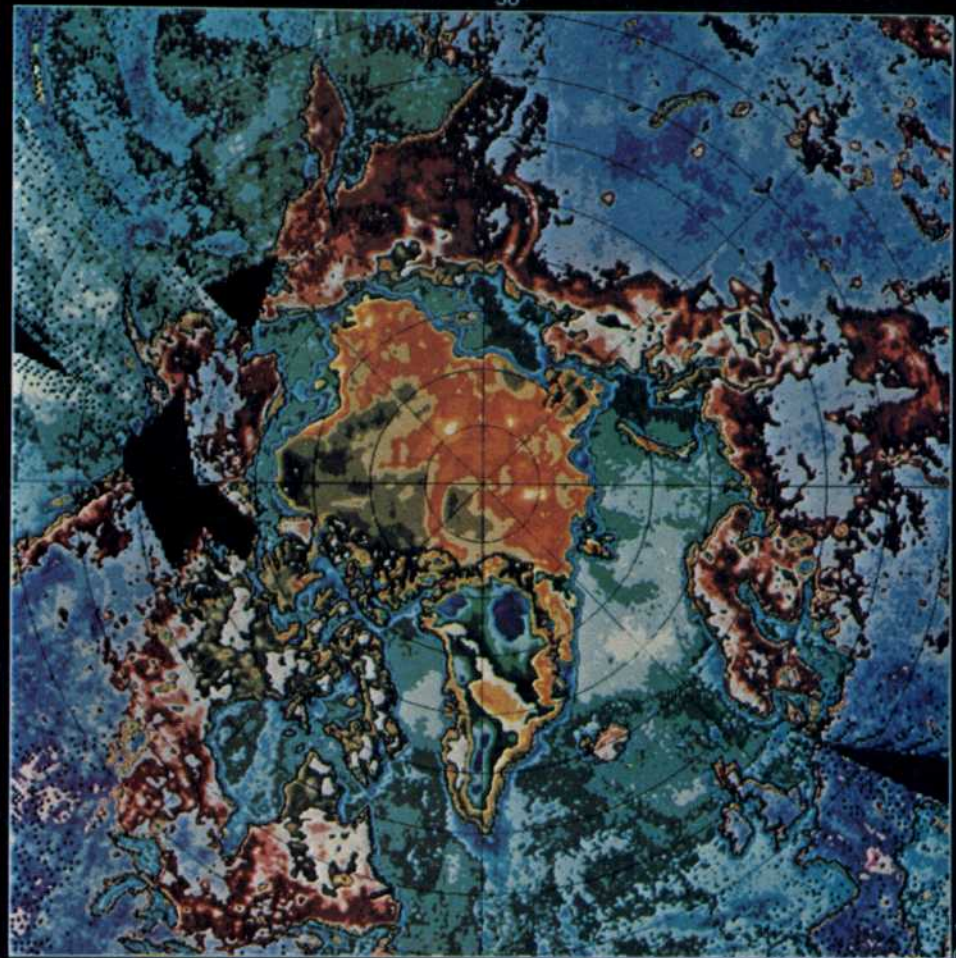
50°



(a)

Fig. 14. Images of north polar region generated from brightness temperatures measured by the Nimbus-5 ESMR: (a) winter (January 1973) (after Zwally and Gloersen [24]).

\*\* NORTH POLAR MICROWAVE BRIGHTNESS TEMPERATURE \*\*  
\* NIMBUS-5 ESMR (1.55 CM) 3-DAY AVERAGE \*  
\*\* SEPTEMBER 9, 73 FROM 252 03 29 TO 254 22 15 \*\*



(b)

Fig. 14. Images of north polar region generated from brightness temperatures measured by the Nimbus-5 ESMR: (b) summer (September 1973) (after Zwally and Gloersen [24]).

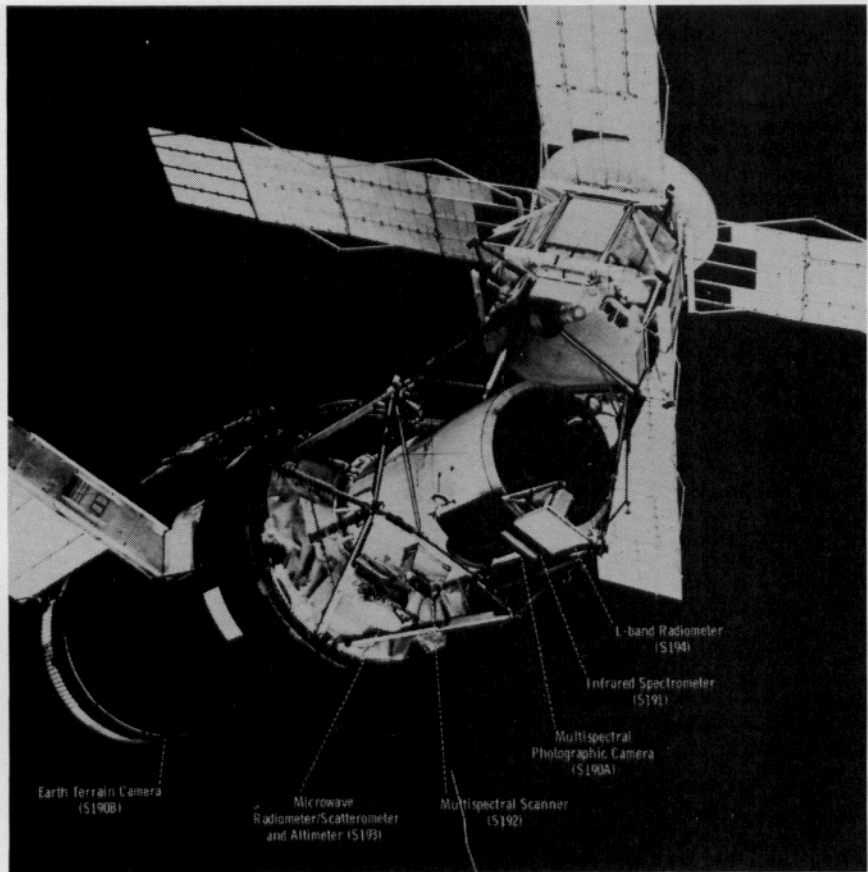
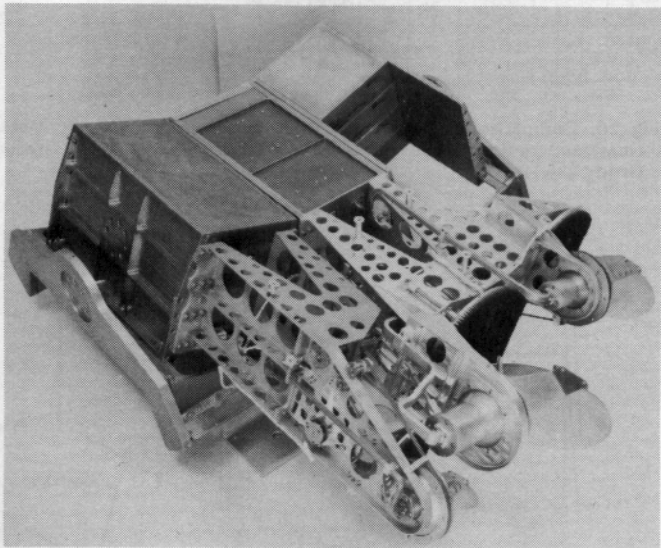
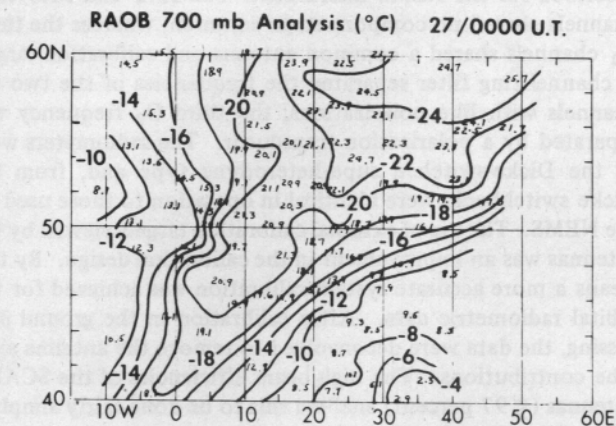
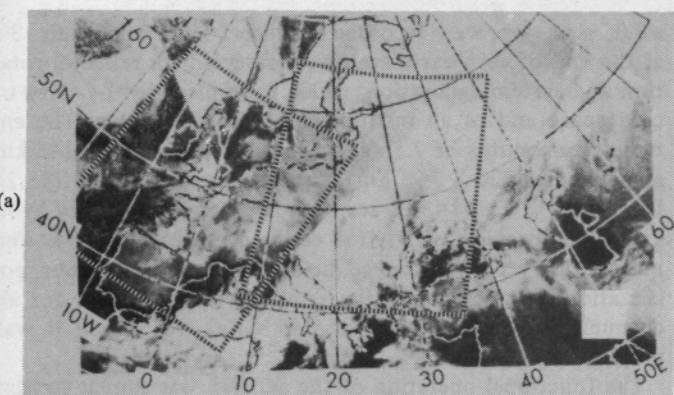


Fig. 15. Skylab, launched May 1973, showing location of EREP sensors on the multiple docking adaptor.



**Fig. 18. Photograph of SCAMS instrument (Nimbus-6).**



NIMBUS-6 SCAMS 700 mb Analysis ( $^{\circ}\text{C}$ )  
Using Theoretical Coefficients 26/2248-27/0038 U.T.

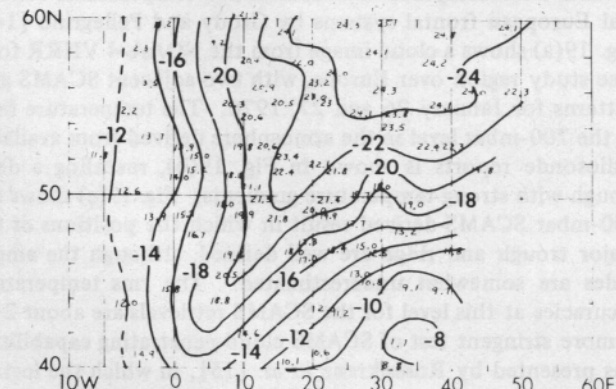


Fig. 19. Comparisons between SCAMS 700-mbar retrieved temperature measurements and radiosonde data, January 26/27, 1976: (a) NOAA-4 VHRR satellite image showing cloud features and SCAMS grid coverage; (b) analysis of 0000 UT radiosonde temperatures; (c) analysis of 2248-0038 UT SCAMS retrieved temperatures (after Grody and Pellegri [14]).

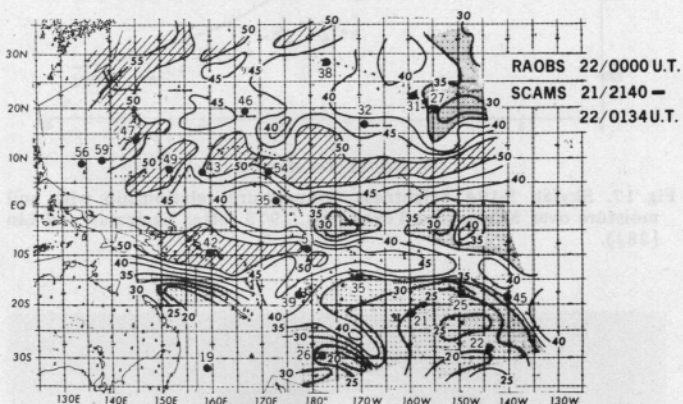
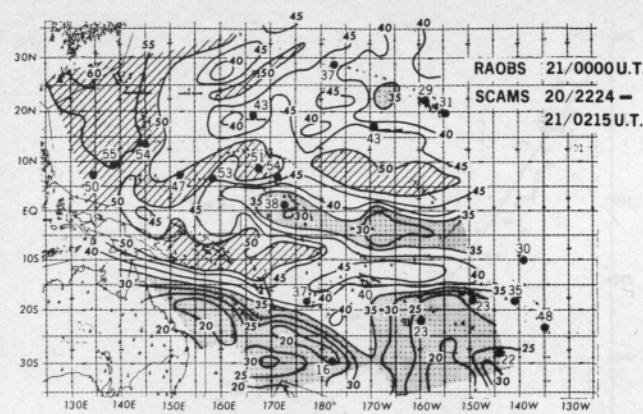


Fig. 20. Comparisons between SCAMS retrieved precipitable water (mm) and radiosonde measurements (●), August 20–22, 1975 (after Grody [10]).

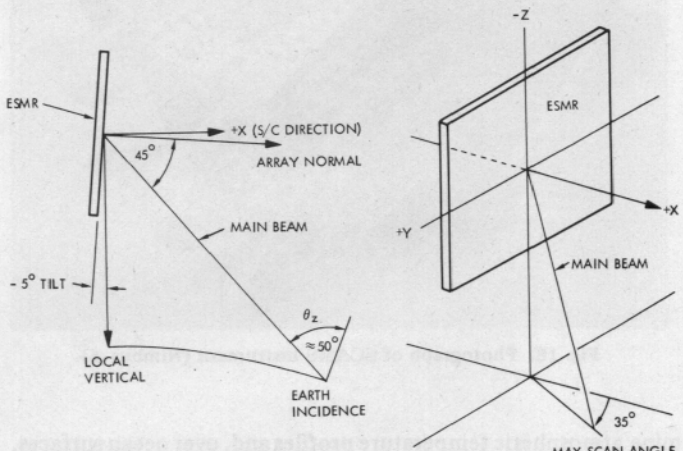


Fig. 21. ESMR (Nimbus-6) antenna scan geometry (after Wilheit [60]).

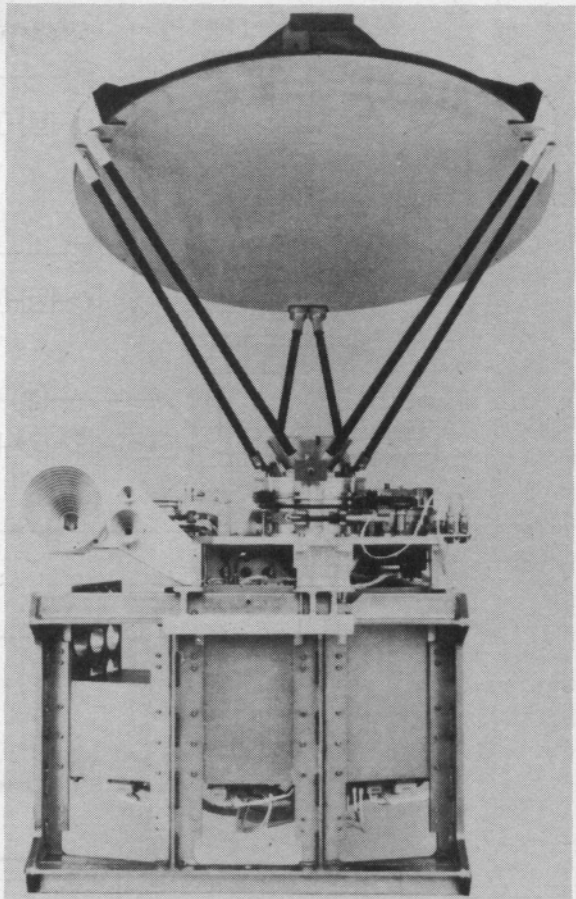
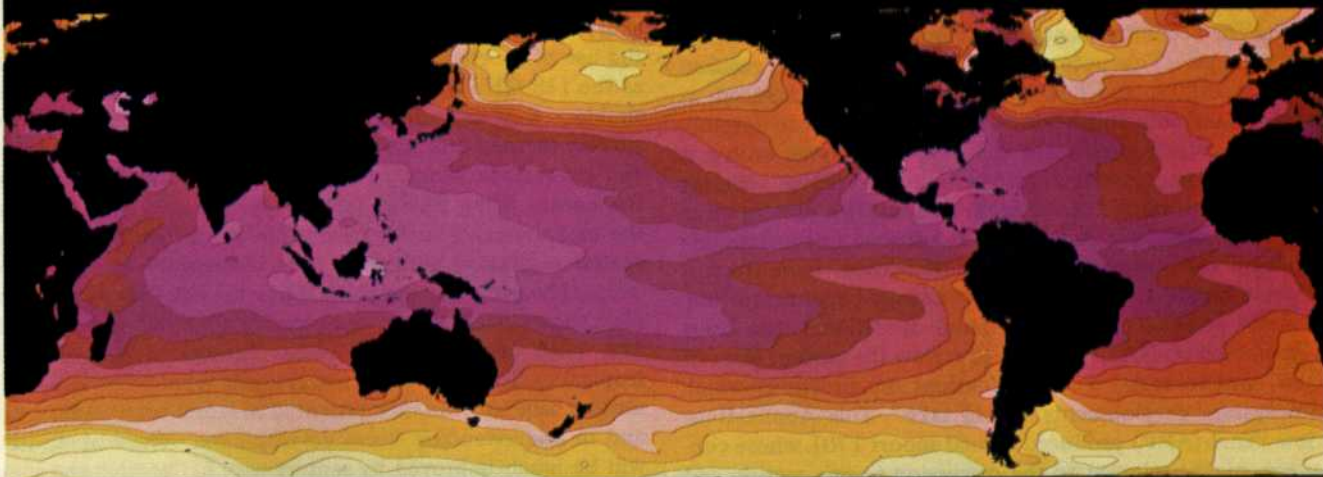


Fig. 22. Photograph showing front view of SMMR instrument (Seasat and Nimbus-7).

SEASAT SMMR SEA SURFACE TEMPERATURE  
JULY 13 - 24, 1978



CHESTER, HUSSEY  
NJOKU AND NICHOLS  
(1981)

DEGREES CENTIGRADE



Fig. 26. Global sea surface temperature contour map derived from Seasat SMMR data, July 13–24, 1978.